

UNIVERSITY OF WATERLOO  
Faculty of Science

**Prototyping and Simulation of the T2K OTR Monitor**

Professor John Martin  
Dr. Alysia Marino  
University of Toronto

Prepared by  
Patrick de Perio  
UW ID: 20170537  
pdeperio@uwaterloo.ca  
3B Mathematical Physics  
December 30, 2007

## Summary

This document outlines the prototyping of the T2K OTR optical system and simulations of beam reconstruction. The purpose of T2K and the OTR monitor is motivated and the principles behind the monitor are described. Assembly of the prototype and the motivations of the design of the optical system are explained. A calibration foil consisting of a grid of holes, similar to what will be used in the full-sized system, was tested in the prototype. Two methods for lighting the calibration foil were tested: front-lighting and back-lighting.

An image processing routine involving hole finding and matching to control points was developed and tested with an image of the calibration foil in the prototype system. A distortion and efficiency correction routine were developed to correct the inherent effects of using parabolic mirrors in the optical system. These routines were tested with real images from the prototype system to an accuracy of 5%. The efficiency correction routines were tested using two different methods of determining the efficiency map, with three different angular distributions of light. They were applied to simulations of an actual distorted beam profile and reconstructed the position and width to an accuracy of 0.05 mm regardless of the method or lighting used. This result is well within the target goal of 0.5 mm for the OTR monitor.

# Contents

<b>List of Figures</b>	<b>iii</b>
<b>List of Tables</b>	<b>v</b>
<b>1 Introduction</b>	<b>1</b>
1.1 Neutrino Oscillation Physics . . . . .	1
1.2 T2K and the OTR Monitor . . . . .	3
1.3 Transition Radiation . . . . .	6
<b>2 Prototyping</b>	<b>8</b>
2.1 Optical Design of the Monitor . . . . .	8
2.2 Calibration Foil . . . . .	11
2.3 Camera . . . . .	12
2.4 System Alignment . . . . .	13
2.5 Lighting . . . . .	15
2.5.1 Front-lighting . . . . .	16
2.5.2 Back-lighting . . . . .	18
2.6 Distortion and Efficiency Falloff . . . . .	21
2.7 Simulation and Hole Finding . . . . .	22
2.7.1 Limitations of Front-lighting . . . . .	25
2.8 Undistortion . . . . .	26
2.9 Efficiency Correction . . . . .	27
<b>3 Beam Reconstruction Simulations</b>	<b>30</b>
3.1 Lighting . . . . .	31
3.2 Undistortion . . . . .	32
3.3 Efficiency Correction . . . . .	32
3.3.1 Efficiency Map produced from a Grid . . . . .	33
3.3.2 Efficiency Map produced from a Uniform Disk . . . . .	35
3.4 Results . . . . .	40

**4 Conclusions and Recommendations 42**  
4.1 Conclusions . . . . . 42  
4.2 Recommendations . . . . . 43

**A Hole Matching Code 46**

**B Diffuse Light and Uniform Cone Code 53**

**C Beam Profiles 55**

**Bibliography 58**

# List of Figures

1.1	Overview of the J-PARC Accelerator . . . . .	4
1.2	T2K Long Baseline . . . . .	5
1.3	T2K Target Area . . . . .	5
1.4	OTR Lobes . . . . .	6
1.5	OTR Angular Distribution . . . . .	7
1.6	OTR Cone . . . . .	7
2.1	Stretched Foil in a Circular Holder . . . . .	8
2.2	Drawing and Schematic of the Optical System . . . . .	9
2.3	Assembled Prototype System . . . . .	9
2.4	A 90° Off-axis Parabolic Mirror . . . . .	10
2.5	Grid Pattern of the Calibration Foil . . . . .	11
2.6	Aligning the Mirrors . . . . .	13
2.7	Finding the Mirror Center . . . . .	14
2.8	Positioning of Back and Front-lighting . . . . .	15
2.9	Fluorescent Ring Lamp . . . . .	16
2.10	LED Ring Efficiency Map . . . . .	17
2.11	Christmas Light Ring Efficiency Map . . . . .	17
2.12	Front-lit Calibration Foil . . . . .	18
2.13	Light Pipe Sources . . . . .	19
2.14	MagLite and Reflector Efficiency Map . . . . .	19
2.15	Distorted Grid with Back-lighting . . . . .	21
2.16	Image Distortion of Graph Paper . . . . .	22
2.17	Light Efficiency Falloff through the Optical System . . . . .	22
2.18	Intensity Maps of the Distorted Grids . . . . .	23
2.19	Grid Distortion Map . . . . .	24
2.20	Front-lit Grid . . . . .	25
2.21	Undistorted Graph Paper . . . . .	27
2.22	Undistorted Grids and Efficiency Maps . . . . .	28
2.23	Intensity Maps of the Efficiency Corrected Grids . . . . .	28
3.1	Angular Distribution of Reflected Light from a Ti Foil . . . . .	31

3.2	Undistorted Beam Positions . . . . .	33
3.3	Efficiency Map Created from a Grid . . . . .	34
3.4	Efficiency Corrected Beam Positions (Grid Map) . . . . .	36
3.5	Error in x using a Grid Efficiency Map . . . . .	36
3.6	Error in y using a Grid Efficiency Map . . . . .	37
3.7	Reconstructed Width using a Grid Efficiency Map . . . . .	37
3.8	Efficiency Corrected Beam Positions (Disk Map) . . . . .	38
3.9	Error in x using a Disk Efficiency Map . . . . .	38
3.10	Error in y using a Disk Efficiency Map . . . . .	39
3.11	Reconstructed Width using a Disk Efficiency Map . . . . .	39
3.12	Efficiency Map Created from an Empty Foil Holder (Uniform Disk) . . . . .	40
C.1	Original Beam Profile . . . . .	56
C.2	Distorted Beam Profile . . . . .	56
C.3	Undistorted Beam Profile . . . . .	57
C.4	Efficiency Corrected Beam Profile . . . . .	57

## List of Tables

3.1	Efficiency Map Characteristics . . . . .	33
3.2	Beam Reconstruction Results 10 mm away from Center . . . . .	41
3.3	Beam Reconstruction Results 2 mm away from Center . . . . .	41

# Chapter 1

## Introduction

### 1.1 Neutrino Oscillation Physics

The neutrino, first observed in 1956 [1], is a fundamental particle of which our current understanding is very limited. It interacts via only the weak force and thus rarely interacts at all. There are three flavours that are currently known: the electron neutrino ( $\nu_e$ ), muon neutrino ( $\nu_\mu$ ) and the tau neutrino ( $\nu_\tau$ ), each of which has a corresponding anti-particle. Originally, the Standard Model described neutrinos as massless. A theoretical consequence of this forbids neutrino flavour change.

However, recent experimental evidence has shown otherwise. For example, our sun theoretically produces a flux of billions of neutrinos per second per  $\text{cm}^2$  at the Earth, accurate from 1% to 23% depending on the neutrino energy [2]. The amount observed however, was in deficit by approximately one-third, consistent across many detectors which were calibrated to observe only  $\nu_e$ . This is known as the solar neutrino anomaly. The Sudbury Neutrino Observatory (SNO) experiment [3] has provided strong evidence for flavour

oscillations, explaining this anomaly and accounting for the missing neutrinos.

Super-Kamiokande, an existing detector which will be used as the far detector for T2K, has also shown evidence for oscillation using atmospheric neutrinos [4]. These are produced by the collision of cosmic rays with particles in the atmosphere. Results show a top-bottom asymmetry in the neutrino counts, attributable to neutrino oscillations that occur as they travel the extra distance through the Earth. Now the neutrinos must be massive for these flavour oscillations to occur, opening a new and deep topic for investigation.

The following is a summary of the discussion given in [5]. The current model of neutrino oscillations has flavour eigenstates of the neutrinos  $\nu_l$  that are a combination of the mass eigenstates  $\nu_i$ :

$$|\nu_l\rangle = \sum U_{li}|\nu_i\rangle \quad (1.1)$$

where  $U_{li}$  is a ‘mixing’ matrix of constants. If the masses of  $\nu_i$  differ, then when a neutrino is created, its mass state  $\nu_i$  is not well-defined and there is a probability of observing different flavours at a later time. For example, the probability of observing a  $\nu_\tau$  from a beam of pure  $\nu_\mu$  is

$$P(\nu_\mu \rightarrow \nu_\tau) = \sin^2(2\theta) \sin^2\left(\frac{1.27\Delta m^2 L}{E}\right) \quad (1.2)$$

where  $\theta$  is one of the three ‘mixing angles’ of  $U_{li}$ ,  $\Delta m^2$  is the difference in the squares of the masses of  $\nu_i$  in  $eV^2$ ,  $L$  is the distance traveled in km and  $E$  is the energy of the neutrino in GeV. Equation (1.2), which involves only two mass states, is a simplified version of the three mass case given in [6]. In both cases, the probability varies with the distance traveled. Using this equation, over hundreds of kilometers, we expect to observe a statistically significant amount of oscillations for 1 GeV neutrinos.

There are several unknown parameters in the mixing matrix, including one of the mixing angles<sup>1</sup>, that describes neutrino oscillations. One of the main goals of the T2K project is to measure the  $\nu_\mu$  disappearance as well as the  $\nu_\mu$  to  $\nu_e$  appearance signal to obtain a value for the unknown mixing angle as well as the  $\Delta m^2$ 's. Measurements of these parameters will lead to a large contribution to the current model of particle physics and insight to the matter-antimatter asymmetry of our universe.

## 1.2 T2K and the OTR Monitor

The Tokai to Kamioka (T2K) project is an international collaboration based in Japan. A proton beam will be redirected from the J-PARC facility shown in Figure 1.1 toward the existing Super-Kamiokande detector in Kamioka. The protons will be smashed into a graphite target, producing mostly<sup>2</sup>  $\pi^+$  and  $K^+$  which subsequently decay into  $\mu^+$ ,  $\nu_\mu$  and a small amount of  $\nu_e$ . The resulting neutrino beam<sup>3</sup> will then travel a distance of 295 km before being measured at Super-K, Figure 1.2.

Canada's involvement is primarily in the near-detector situated 280 m downstream of the target. Its main purpose is to obtain an initial profile of the beam to make predictions for what should be observed at the far detector in Kamioka in the absence of oscillations. The efforts at the University of Toronto, York University and TRIUMF however, are focused on developing an Optical Transition Radiation (OTR, refer to Section 1.3) monitor that sits immediately upstream of the target as shown in Figure 1.3.

---

<sup>1</sup>The other two angles are known from solar and atmospheric neutrino measurements.

<sup>2</sup>Some negative particles are also created, but these are focused away from the beam line by the horns (Figure 1.3).

<sup>3</sup>The  $\mu^+$  is absorbed by the surrounding rock and does not follow the neutrino beam line.

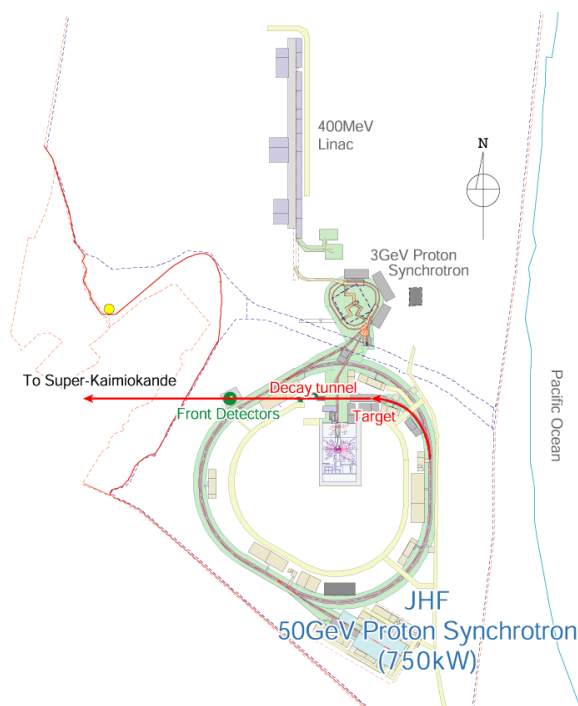


Figure 1.1: This map shows the system of accelerators from which the proton beam is produced in Tokai, Japan.

The purpose of the monitor is to measure the position and width of the proton beam just before it strikes the target. Following the target are three magnetic horns which bend the trajectories of particles that are not parallel to the beam axis and are off-center. So if the beam position is off, the overall beam direction will change accordingly, affecting the neutrino spectrum observed at Super-K. This effect can be estimated but requires the position of the proton beam at the target to be measured with a precision of 1 mm. The simulations in this document use a Gaussian beam of 30 GeV protons with a width of 7.5 mm, comparable to what will be used in the real system. A larger beam width will irradiate too much material surrounding the target while a smaller beam width will increase the energy density of the beam and damage the target. Thus the width must also be measured with a precision of 0.5 mm.



Figure 1.2: T2K Long Baseline

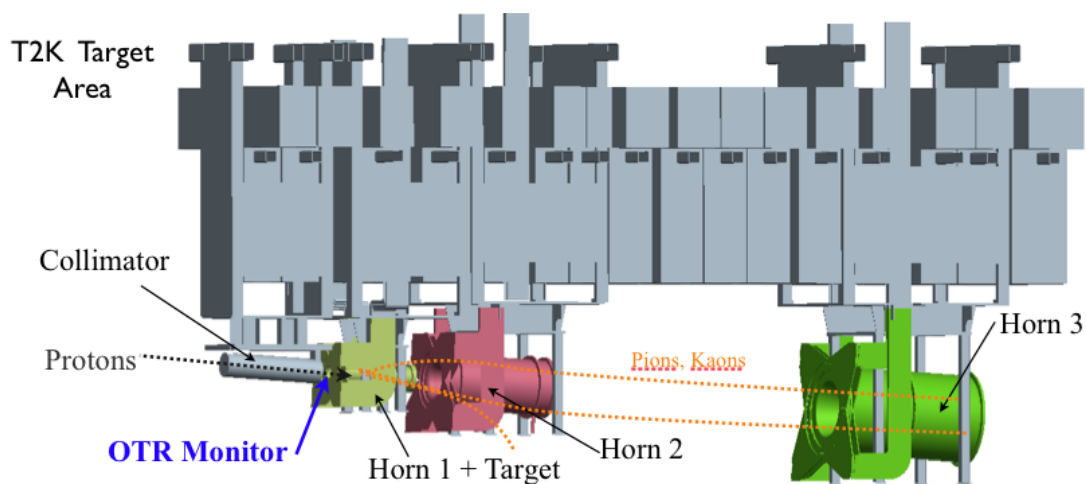


Figure 1.3: This drawing shows a side view of the T2K target area. The proton beam travels to the right and interacts with the OTR monitor immediately after the collimator and before reaching the target. The horns are magnetic devices which act to focus the beam in the right direction. The grey part above the OTR monitor is the concrete and iron shielding through which the OTR light must be transported.

Placing any electronics near the beam path at the target is challenging. The target area is highly radioactive and will also damage any nearby electronics. Fortunately, light is produced as a proton passes through a thin foil (OTR). This light can be directed away from the target area and then collected to produce an image with information about the shape, size and position of the beam.

### 1.3 Transition Radiation

Transition radiation is produced by a charged particle crossing the boundary between two media with different dielectric constants. The difference of the electric field of the particle in each medium is accounted for by the emission of this radiation [7]. It is calculated in [8] that only a thin layer (a couple microns) of metal is required to produce transition radiation. Some of the light that is emitted travels in the forward direction, which is difficult to collect as it follows the beam path. However, some light is also reflected backward along the reflection axis. Figure 1.4 shows how the light can be redirected away from the beam axis.

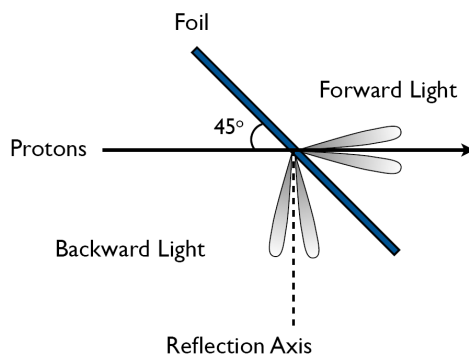


Figure 1.4: This drawing shows the lobes of light produced when a beam of protons travels through a foil positioned at  $45^\circ$  to the beam axis.

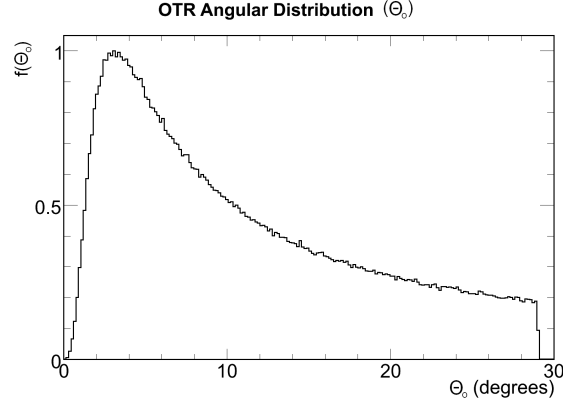


Figure 1.5: This plot shows a distribution of randomly generated angles according to Equation 1.3, for a 30 GeV proton. The tail-end is cut off because light with angles greater than  $30^\circ$  will hit the walls of the monitor and be useless in simulations.

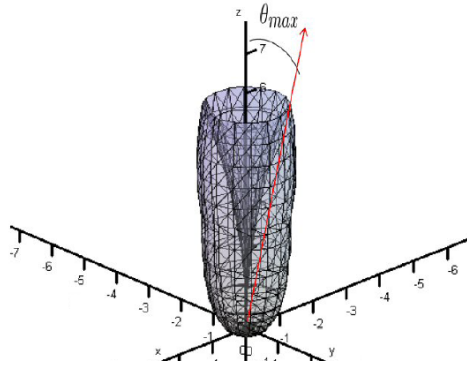


Figure 1.6: This plot shows one of the lobes of Figure 1.4 in greater detail, where  $\theta_{max}$  denotes the direction of highest intensity. It is essentially a revolution of Figure 1.5 about the y-axis.

The direction of light actually surrounds the reflection axis with the polar angle<sup>4</sup>,  $\theta_o$ , following a distribution given by

$$f(\theta_o) = \frac{\theta_o^2}{(\gamma^{-2} + \theta_o^2)^2} \sin \theta_o \quad (1.3)$$

where  $\gamma \approx 32$  for a 30 GeV proton, plotted in Figure 1.5. The azimuthal angle is uniform from 0 to  $2\pi$ , forming the hollow cone-like distribution shown in Figure 1.6.

---

<sup>4</sup>The angle between the direction of the photon and the reflection axis.

## Chapter 2

# Prototyping

### 2.1 Optical Design of the Monitor

The proton beam will strike a 50 mm diameter foil (Figure 2.1) at  $45^\circ$  to produce reflected light as described above. The collimator that the beam exits from is 30 mm in diameter. This area is projected onto the effective area of the foil rotated at  $45^\circ$ . A system of four mirrors is used to transport the OTR light through the shielding as shown in Figure 2.2(a). This prevents a direct path through which radiation can escape and also allows the placement of a camera and electronics in a more radiation-safe environment



Figure 2.1: A thin stainless steel foil stretched in a stainless steel circular holder. The actual foils will be a titanium alloy (15-3-3-3).

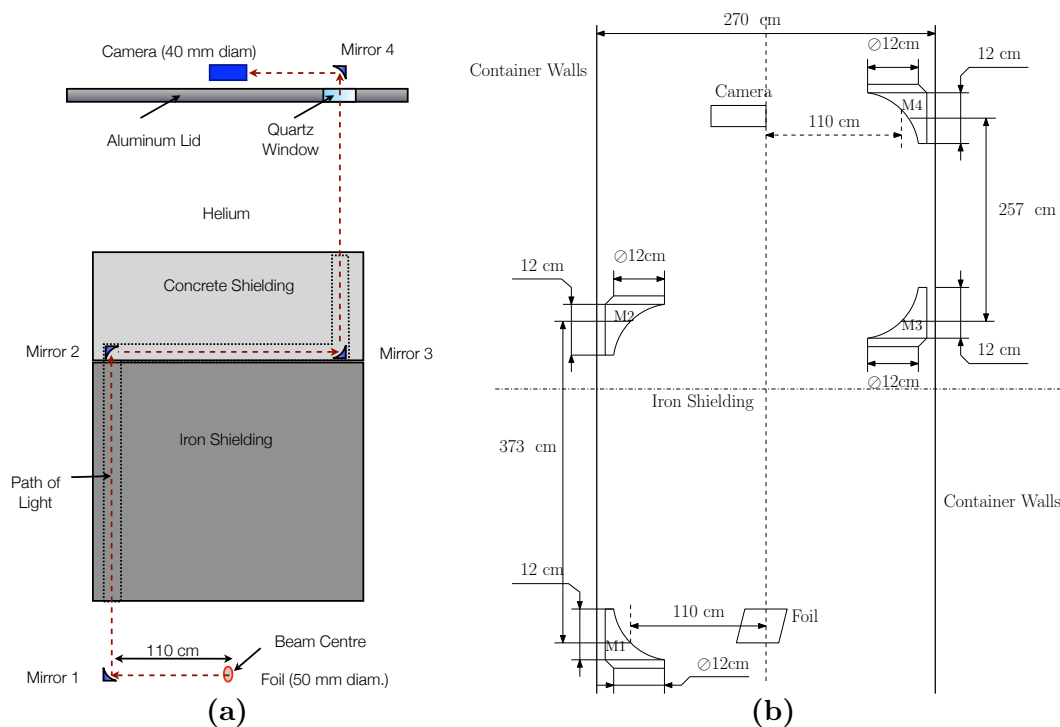


Figure 2.2: (a) This drawing shows the path of OTR light. It is produced at the foil with the proton beam traveling into the page and the foil at  $45^\circ$ . (b) The mirrors in this schematic all have parent focal lengths of 55 cm. However the focal length of mirror 4 will be approximately 30 cm to shrink the image of the 50 mm foil onto a 40 mm diameter camera. The distance between mirror 4 and the camera will change accordingly.

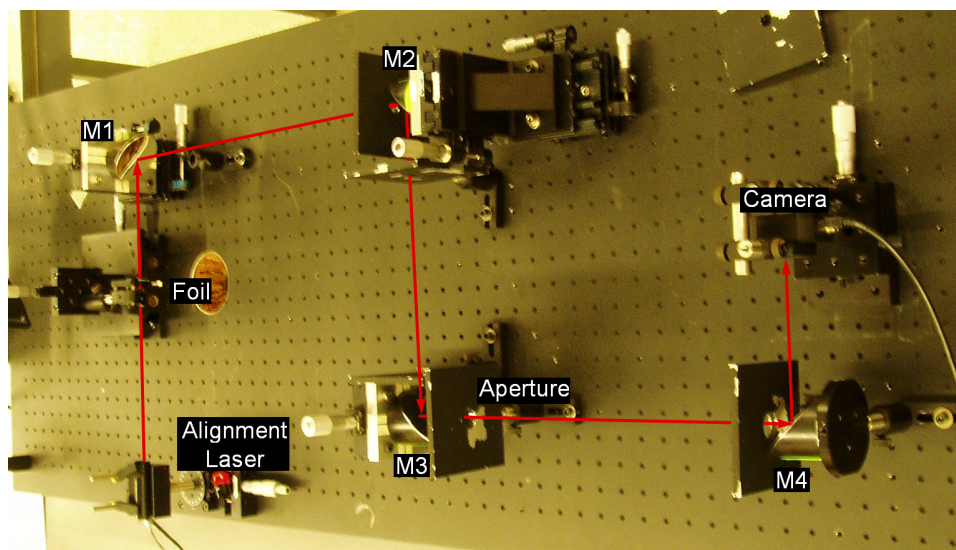


Figure 2.3: This photo shows an overview of the assembled prototype system with the path of the alignment laser (Section 2.4). Note that the system is lying horizontal whereas the full-sized system is vertical.

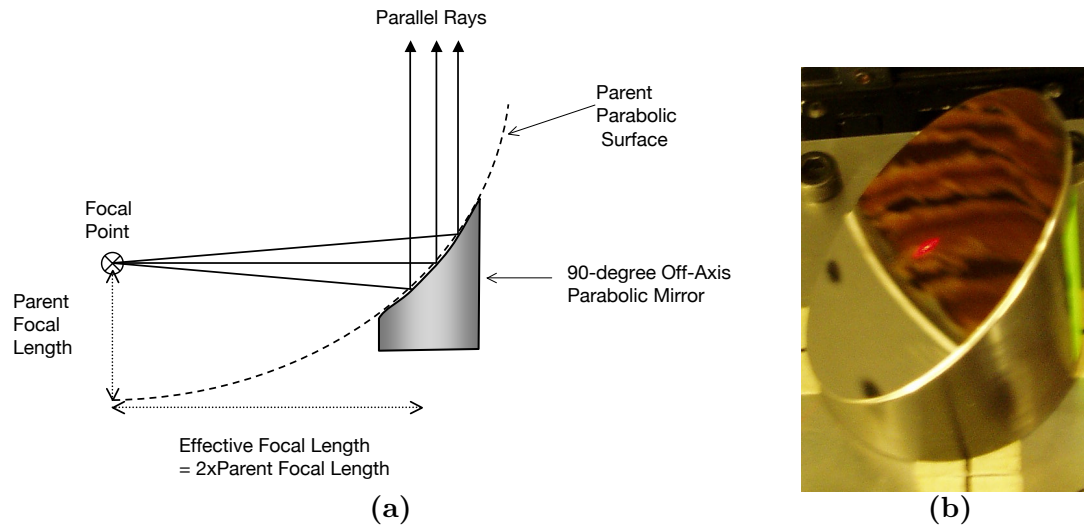


Figure 2.4: (a) A drawing demonstrating the focusing of rays from the focal point. (b) A mirror used in the prototype system.

outside the target area. In order to collect a sufficient amount of light and focus it onto the camera,  $90^\circ$  off-axis parabolic mirrors are used (Figure 2.4). These mirrors can recover light at stray angles that flat mirrors cannot.

Mirror 1 is placed as far as possible from the foil to minimize its exposure to radiation and prevent a loss of reflectivity. All the mirrors are the same diameter as mirror 1 at 12 cm, which is large enough to collect most of the light from the foil. The effective focal length (twice the parent focal length) must be equal to the distance between the foil and mirror 1 for proper focusing (see Figure 2.2(b)). A prototype optical system has been assembled. The dimensions are scaled down to 15% aside from the mirror diameters which are 5 cm in the prototype system. This difference is insignificant once the appropriately sized apertures are installed because any extra light collected by the edges of the prototype mirrors will cut off by the apertures. The apertures in the prototype system mimic the pipes that will be in between mirrors 1 and 2 and mirrors 3 and 4.

## 2.2 Calibration Foil

The foils that the proton beam will hit must be solid for mechanical strength. Any image obtained from them will have no reference to real (foil) space so the system must be initially calibrated. Images are compared to a foil with markings at known positions in order to extract any useful information. The full-sized system will employ an array of foils, one of which will be this calibration foil. The foil used in the prototype system is shown in Figure 2.5, which is not necessarily the same pattern that will be used in the full-sized system. After passing through the optical system, the image of the holes in camera space can be matched to the known positions in foil space. Using this matching, when an actual image of the beam is obtained, it can be reconstructed to the correct position in foil space as required.

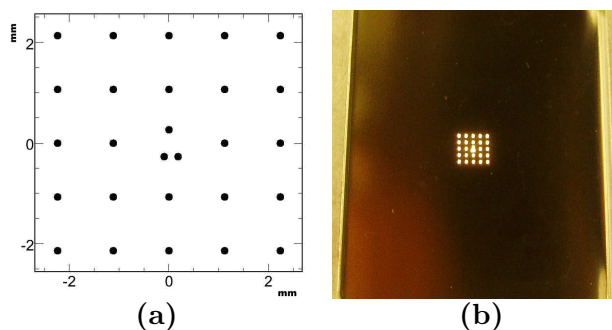


Figure 2.5: (a) The grid design consists of 100  $\mu\text{m}$  diameter holes with horizontal spacing of 1.12 mm and vertical spacing of 1.07 mm. The center hole was replaced with a triangle to assist in the hole finding routine (Section 2.7). (b) The pattern was laser machined into a 0.002" stainless steel foil with positions within 10  $\mu\text{m}$  of specification and  $110 \pm 5 \mu\text{m}$  in diameter.

The grid is rectangular, designed to fit the camera used in the prototype system. The triangular center pattern is designed to provide orientation as it passes through the optical system as well as assist in the hole finding routine (Section 2.7) which recognizes

the triangle as the center of the grid.

## 2.3 Camera

The viewable region of the CCD camera used for prototyping is 6.56 mm wide by 5.25 mm (8.4 mm diagonal, 1280 by 1024 pixels). It measures the amount of red, green and blue light (on a scale of 0 to 65535) at each pixel and outputs a .bmp file with the data. Noise in the camera is more apparent at lower light levels. Also, at exposure times less than 17 ms<sup>1</sup> the bands due to interference between the camera readout timing and an AC light source become undesirably visible. So either a DC source or a longer exposure time must be used. However, with longer exposure times the level of light must be kept low enough such that the camera does not saturate (white areas in the image) giving inaccurate intensity readings.

Uniformity in the camera output was tested by placing a diffuse light source (Christmas light ring, Section 2.5.1) far away (1.5 m). The level of light was varied from zero to the saturation point of the camera by adjusting the power delivered to the ring. The intensity values across the resulting images were calculated to be uniform to more than 99%. A single hot pixel was found but is drowned out by any surrounding lighted pixels. If it is surrounded by dark pixels it will be ignored by the subsequent hole finding routine. A vertical line of semi-hot pixels was observed at extremely low intensities and seemed to vary in position with time. This suggests some noise in the camera readout, but fortunately it is insignificant in the presence of any light.

---

<sup>1</sup>Corresponding to a 60 Hz AC light source.

## 2.4 System Alignment

The shape of the distortion and efficiency falloff (described in Section 2.6) are sensitive to the alignment of the foil, mirrors and camera. Translation of the foil across the optical axis can result in the side of it being cutoff at the camera. Translation of the camera can result in the image being centered somewhere around the edge of Figure 2.17. This can be corrected, however more light is being lost than if it was aligned properly. These effects are even more apparent with misalignments of the mirrors, rotations being much more dramatic than translations. A detailed study on the effects of mirror misalignment is given in [9].

In the interest of comparing the prototype to simulations, which have a perfectly aligned system, it is desirable to align the centers of the foil, mirrors and camera to the optical axis. For the full-sized system, proper alignment is even more important for the unlikely event that the physical calibration fails and we must rely on simulations.

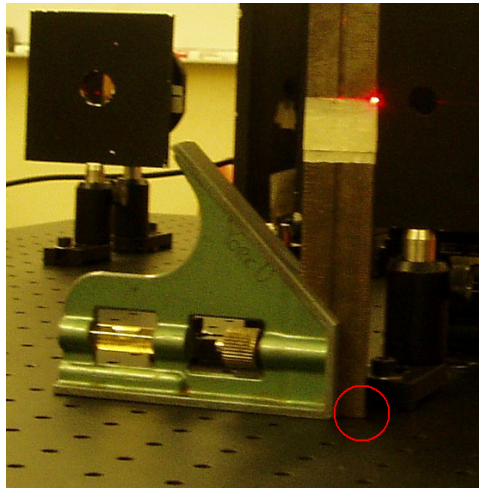


Figure 2.6: This photo shows the ruler used to block the laser in order to align it and properly adjust the mirrors. The circled corner of the ruler is placed in the center of a hole in the optical table.

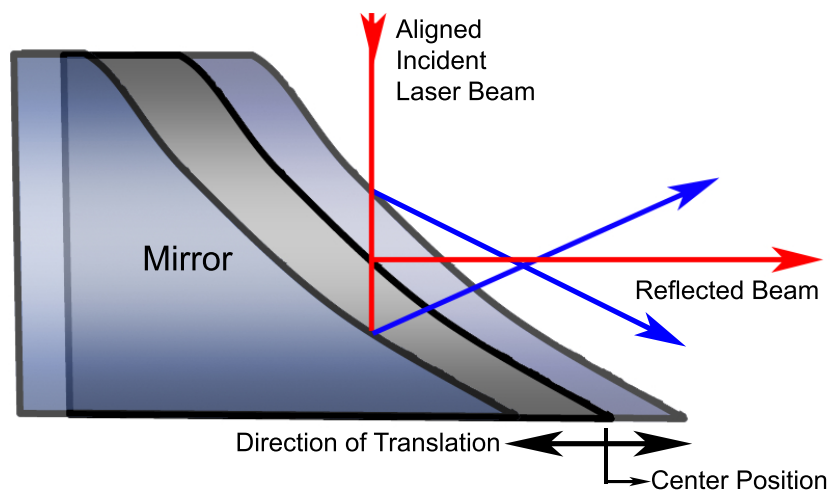


Figure 2.7: This drawing shows how the center of a mirror is found by translating it across the beam axis. The blue rays show the direction of the laser reflecting off a non-center point.

The alignment laser is leveled vertically by ensuring it is at the same height across the table. It is aligned to the holes in the table by using the vertical ruler shown in Figure 2.6. The ruler is placed in front of the laser with the edge centered on a hole in the optical table. The laser is adjusted so that half the beam is blocked by the ruler. This procedure is repeated at the opposite end of the table to ensure that the laser is aligned to the holes.

The prototype mirrors are aligned sequentially, before the camera and the foil, by ensuring the laser hits the center of each mirror. Starting with mirror 1, the height is adjusted until height of the reflected beam is constant over the length of the table. Assuming the mirror is mounted at exactly  $90^\circ$ , the center can be found by translating the mirror across the laser axis until the beam reflects at  $90^\circ$  as shown in Figure 2.7. Since the laser is initially aligned to the holes of the table, at  $90^\circ$  the reflected beam should still be aligned to the holes and can be checked in the same manner as above. This procedure is repeated

for the remaining 3 mirrors. The camera is aligned by centering the image of the laser beam on the computer screen which monitors the camera output. Finally, the calibration foil is adjusted until the laser beam hits the center of the triangle pattern, which can be positioned precisely using the camera output on the computer screen.

## 2.5 Lighting

The target area will be dark and so a light source is required to illuminate the calibration foil. Due to the high radiation, conventional light sources cannot be used. Some other possible light sources include radiation-hard filaments or a ‘light-pipe’ leading into the target area through which light can be injected from above the shielding. There are two methods of lighting the foil, as shown in Figure 2.8.

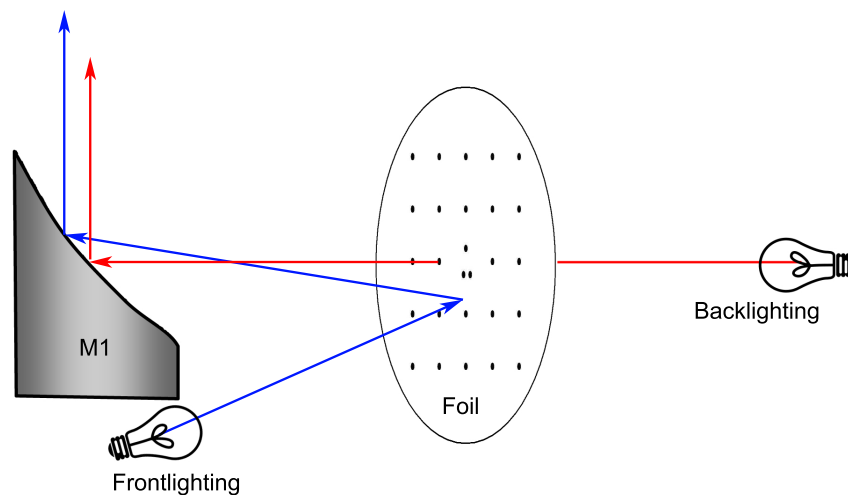


Figure 2.8: In the full-sized system, for front-lighting, an array of filaments will replace the light-bulb symbol. For back-lighting, a diffuse reflector will replace the light bulb, with filaments or a light-pipe pointing at it. In the prototype system, it is sufficient to use the Christmas light ring for front-lighting (Section 2.5.1) and the MagLite with reflector for back-lighting (Section 2.5.2).

The uniformity and angular distribution of the light emanating from the foil,

whether it be back or front-lighting, is important to know for later efficiency corrections (Section 2.9). For the prototype, several light sources, not necessarily applicable to the full-sized system, were tested. Unless stated otherwise, the efficiency maps shown in this section were obtained by replacing the foil in Figure 2.8 with the camera. The 1 on a  $z$ -scale corresponds to the maximum intensity value of that specific image.

### 2.5.1 Front-lighting

For prototyping, it is desirable to use a ring type light source for front-lighting. Positioning a sufficiently large ring in front of mirror 1, pointing toward the foil, will not block the optical path. Also, the mirror will not block much of the incoming light if the ring is placed behind.

The first source tested was a conventional fluorescent lamp as shown in Figure 2.9. There is a discontinuity in the light ring where the bulb is mounted. This produced a visible gradient on the foil making it an undesirable light source.

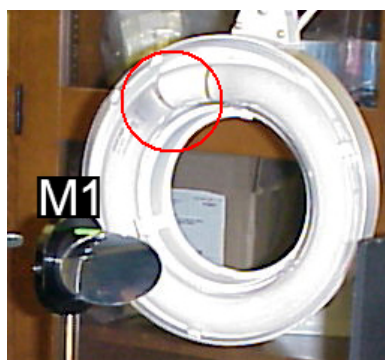


Figure 2.9: This photo shows a conventional lab ring lamp with the discontinuity in the ring circled.

The LED ring, shown in Figure 2.10(a), consists of eight uniformly spaced, white LEDs. The LEDs themselves are very directional and must be adjusted to aim toward the

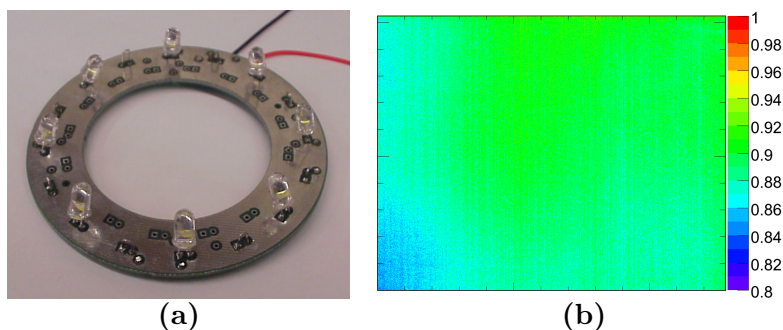


Figure 2.10: (a) This photo shows the LED ring provided by TRIUMF. (b) The corresponding efficiency map shows a 10% gradient.

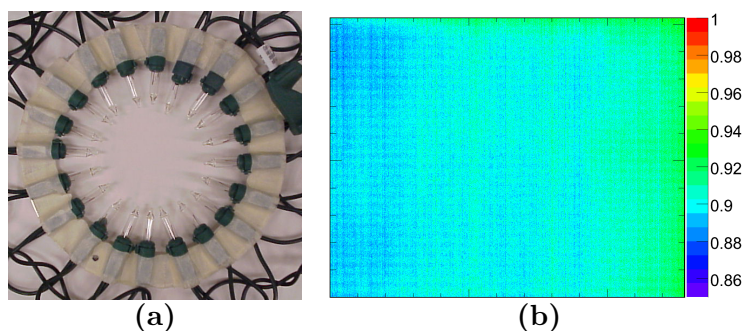


Figure 2.11: (a) This photo shows the Christmas light ring assembled by the author. (b) The corresponding efficiency map shows a 4% gradient with the irregularities in the image caused by noise in the camera.

center of the foil to produce a region of uniform light. The LEDs are not very diffuse and so this region was not very large compared to the foil. A difference in light intensity on the foil is easily observed when a single LED is misaligned. The dark region in the bottom left corner of Figure 2.10(b) shows the effect of a poorly aimed LED ring.

A more diffuse and non-directional source of light is provided by a ring of twenty Christmas lights. This ring provided a much more intense source of light over a wider area. Disregarding the noise of the camera in Figure 2.11(b), the lighting across the foil was uniform to more than 96%.

Front-lighting of the prototype calibration foil in Figure 2.5(b) results in a surpris-

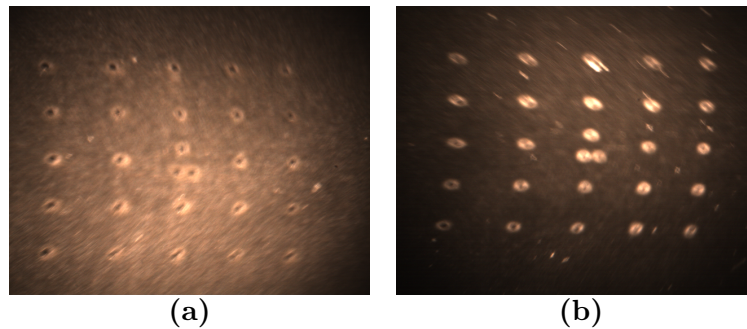


Figure 2.12: (a) This is an image of the concave side of the calibration foil being front-lit. (b) Convex side. Some holes are less blurry and more in focus than others due to the foil's rotation; the position of some of the rows of the holes are no longer at the focal point.

ing observation. A foil imaged with front-lighting, should appear bright with the holes dark since there is no material at those points to reflect light into mirror 1. However, the image of a foil rotated at  $45^\circ$  appears as shown in Figure 2.12. The rings of light are reflected from the edges of the holes while the background remains relatively dark since most of the light is reflected away from mirror 1. The difference in Figure 2.12(a) and Figure 2.12(b) is due to a non-uniformly stretched foil in a rectangular holder. The concave side reflects more light into mirror 1 while the convex side reflects light away. This stresses the importance of using a circular foil holder.

These ring sources are unsuitable for back-lighting due to their relatively large angular distribution. When placed behind the foil, the result is a limited amount of light that passes through the holes and reaches mirror 1, resulting in images with poor contrast.

### 2.5.2 Back-lighting

Back-lighting requires that the light be well-collimated compared to the ring sources. A laser light could provide this as long as it is spread out enough to create a uniform region of light. Shining a laser directly onto a diffuse reflector, shown in Figure 2.14(a),

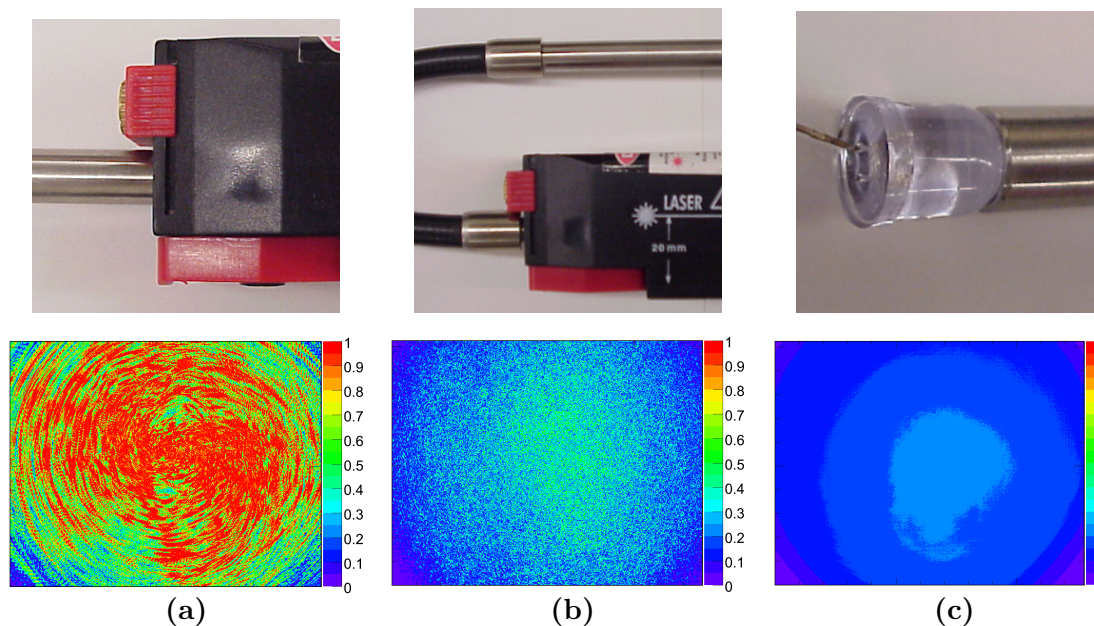


Figure 2.13: These efficiency maps, sharing the same z-scale, were taken 2 cm away from the end of the pipe. (a) A laser shining directly into the pipe and the corresponding efficiency map. (b) A laser passing through a fiber optic cable before entering the pipe. (c) A blue LED shining directly into the pipe, the intensity of which is too low to be of any use in the optical system.

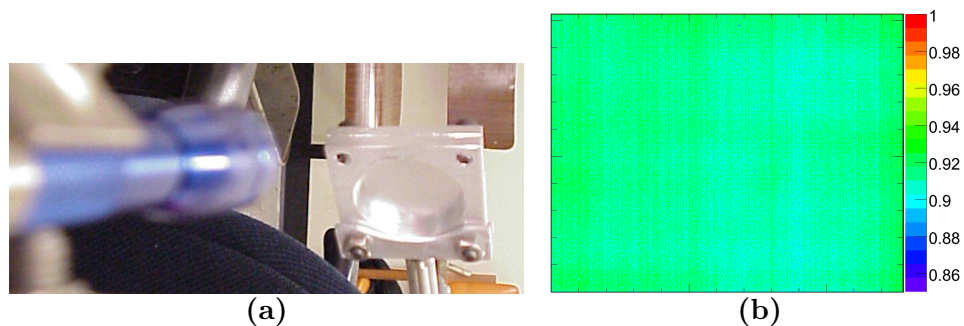


Figure 2.14: (a) The MagLite (left) was placed 0.4 m away from the reflector (right) at  $45^\circ$ . The reflector, made of dull aluminum foil, was 1 m behind the calibration foil in the optical system. (b) This intensity map, imaged at the position of the calibration foil, shows greater than 99% uniformity aside from noise in the camera.

spreads the light but not enough to prevent a visible dropoff in intensity around the edges of the foil. This is improved by shining the laser through a stainless steel pipe, 1.7 m long and 7.5 mm inner diameter, before reaching the reflector. This light-pipe is a possibility for the full-sized system, except it will be approximately 4 m long. However, there are some undesirable interference effects with using laser light. The light exiting the pipe is imaged and shown in Figure 2.13(a). The radial interference pattern is due to the coherent laser light reflecting off the sides of the pipe. To try to improve this, a fiber optic cable is placed between the laser and the pipe as shown in Figure 2.13(b). In the full-sized system, this fiber optic cable would be used to maneuver light through the aluminum lid at the top of Figure 2.2(a). An interference pattern is still visible which creates local irregularities in the lighting across the foil. This results in non-uniform lighting of the holes in the foil and the possibility of some holes not being illuminated at all.

The best back-lighting source for the prototype system is a MagLite, replacing the light-pipe, pointing at the reflector (Figure 2.14(a)). It is essentially a filament within a parabolic reflector which can be easily duplicated in the full-sized system. The parabolic reflector takes most of the light from the filament and focuses it into a semi-collimated source of light. The diffuse reflector then spreads this light out more to create a large area of uniform light (Figure 2.14(b)) that is still relatively collimated to be able to reach mirror 1.

Using the MagLite and reflector to back-light the foil (Figure 2.15) produces a higher contrast image with better defined holes compared to the previous front-lit images. This suggests that back-lighting will be the primary calibration light source in the full-sized

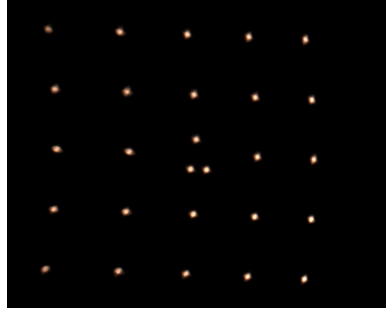


Figure 2.15: This image is of the foil in Figure 2.5 under back-lighting after it passes through the optical system. The slight rotation of the grid is due to foil not being properly aligned in the machine during laser machining. This misalignment can also be observed in the change of the vertical position of the grid in Figure 2.12.

system while front-lighting will be used mostly as a backup.

## 2.6 Distortion and Efficiency Falloff

The grids in the front and back-lit images are not straight and show some warping. This distortion, more clearly observed in Figure 2.16, is an effect of the asymmetry of the parabolic mirrors. This causes a problem when trying to match the positions in camera space to foil space, but as long as the grid holes in foil space are known this distortion can be corrected for (Section 2.8). The image is affected more in the horizontal direction<sup>2</sup> with the warping more pronounced on the points of the image that are further from the center. The distortion will also increase the blurriness of the image, which is not so apparent on the scale of the prototype system.

Another effect of the parabolic mirrors is a falloff in the amount of light collected at the camera moving away from the center of the image. This can also introduce a bias in the position and width of images of the beam. Figure 2.17 was imaged with the same

---

<sup>2</sup>The prototype optical system is rotated 90° to lie on its side while the camera remains upright, so this distortion will appear vertical in the full-sized system.

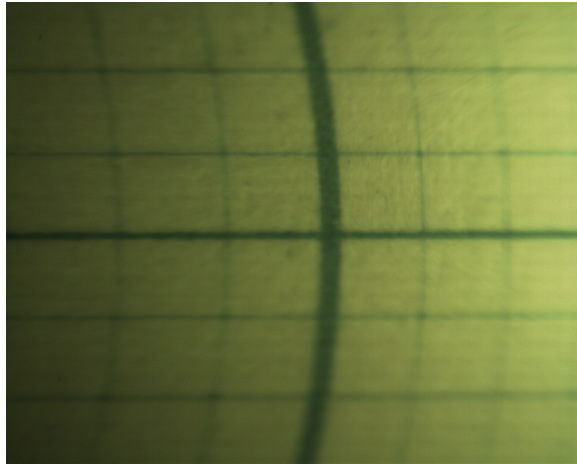


Figure 2.16: This image shows the distortion of straight graph paper through the prototype optical system.

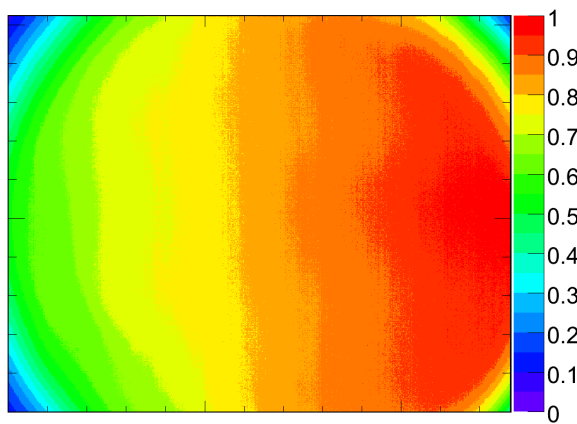


Figure 2.17: This is an image of a uniform light source passing through the prototype optical system.

uniform light source that was used for Figure 2.15, by replacing the calibration foil with an 11 mm aperture (mimicking an empty foil holder). This image will be used later to correct for the efficiency drop in other images (Section 2.9).

## 2.7 Simulation and Hole Finding

Simulations provide a theoretical prediction for the images obtained in the real system. The full-sized system is simulated using ray-tracing software [V. Galymov, York

University]. The same software is implemented with the parameters altered to match the dimensions of the prototype system exactly. The software works by taking a ray with initial position and direction and calculating its intersection with mirror 1. If the position of the ray at mirror 1 lies within the diameter of the mirror, it then calculates the new reflected direction, otherwise it ignores the ray. At the following aperture, it calculates the position of the ray and ignores it if it lies outside the hole of the aperture. Otherwise, the ray continues on to the next aperture and the process is repeated for all the apertures and mirrors in the system until it is accounted for at the camera position. The control grid in Figure 2.5(a) is defined as the source of light rays. These light rays are inputted into the program to produce Figure 2.18(b). The shape of the distortion in the prototype system agrees very well with the simulation.

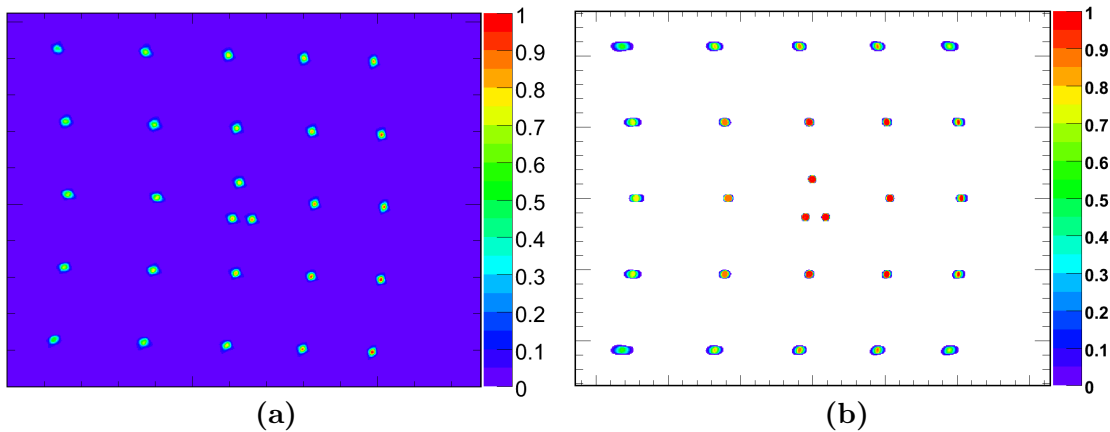


Figure 2.18: (a) Image taken from the prototype system corresponding to Figure 2.15. (b) Simulated image. White space corresponds to a 0 intensity value.

The data provided by these images is simply a number at each pixel corresponding to the intensity value at some position  $(x,y)$ . The background of the prototype image is removed using an adaptive thresholding routine [9] which calculates a threshold intensity

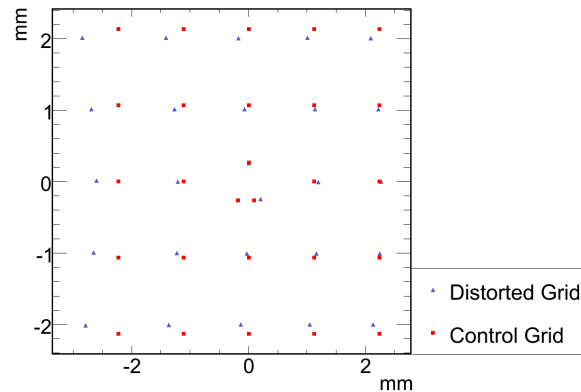


Figure 2.19: The ‘Distorted Grid’ is an example of the centroid positions of holes after running Figures 2.18(a) or 2.18(b) through the hole finding program. The ‘Control Grid’ corresponds to Figure 2.5(a).

value less than the intensity of the pixels in the holes, then sets every pixel below it to 0 (Figure 2.22(a), top). The hole finding routine [9] then groups the remaining, neighbouring pixels into ‘holes’. Real holes are distinguished from irregularities in the foil and noise by ignoring groups of pixels that do not satisfy the criteria for the expected size and intensity of a hole. The centroid position is calculated by a weighted average of the intensity within the hole.

A pattern recognition routine (Appendix A) was written to find the center triangle of holes, distinguished by their close proximity to each other compared to the other grid holes. The position of the center of the triangle is calculated and labeled as the center of the grid. Working outward, the program finds the neighbouring hole based on proximity, and labels it with the corresponding row and column number. With this information, each hole in distorted camera space can be matched with the corresponding control hole in foil space to produce a distortion map (Figure 2.19).

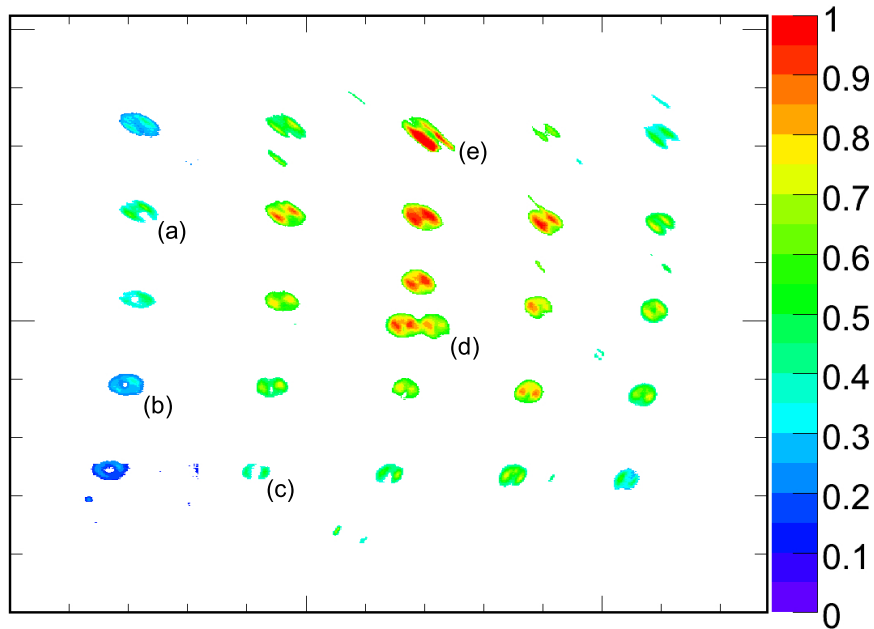


Figure 2.20: This image shows the effect of the adaptive thresholding routine performed on the front-lit foil in Figure 2.12(b).

### 2.7.1 Limitations of Front-lighting

When applying the adaptive thresholding routine on the front-lit grid in Figure 2.12(b), the best image obtained is shown in Figure 2.20. Since the rings produced by the edges of the holes are not very uniform nor consistent (probably from machining imperfections), several problems arise in the hole finding routine. The ring of hole (a) (of Figure 2.20) is cut off at the side, resulting in a biased hole position toward the opposite side. With rings like of hole (b), where the center is clear, the routine can still calculate an accurate centroid position. However, any shift of the ring will bias the position as with (a). Some rings, (c), become cut completely and are ignored in the routine. The angular spread of light reflecting from the edges of the holes results in a ring of light with a much larger area than the hole itself. This increases the blurriness caused by the optical system, conjoining the two holes in the center pattern (d). The pattern recognition routine would

have to be re-written to accommodate for this. The foil is rotated at  $45^\circ$  so the top row is much closer to mirror 1 than the effective focal length. These holes (e) become unfocused, compounding on the previous blurring.

This suggests that the use of front-lighting will be very limited in the full-sized system. Even if an annealed (singed) foil was used in an attempt to avoid the above complications, the contrast of the image will still be poor since the background is dark. The back-lit image is used in favour of the front-lit image for the following analysis.

## 2.8 Undistortion

The undistortion routine basically takes points in a distorted image and translates them to undistorted space using a pre-determined polynomial mapping. To determine this mapping, let  $\{x_k, y_k\} \in f$  be a set of coordinates of control points in undistorted space and  $\{u_k, v_k\} \in g$  be the corresponding set in the distorted image, as in Figure 2.19. Let  $M : f \rightarrow g$  be the transformation matrix which translates any point  $(u, v)$  in distorted space into undistorted space according to the Nth order power series expansion:

$$u = \sum_{i,j=0}^N K_{ij}^{(1)} x^i y^j \quad (2.1)$$

$$v = \sum_{i,j=0}^N K_{ij}^{(2)} x^i y^j \quad (2.2)$$

where  $K_{ij}$  are co-efficients defining the matrix. Using  $\{x_k, y_k\}$ ,  $\{u_k, v_k\}$  and the method of least squares, these coefficients can be calculated [10]. A more accurate but complicated routine, the Weighted Least-Squares Method described in [10], is used instead in the following analyses. It follows the same idea but gives a larger weight to the calibration points

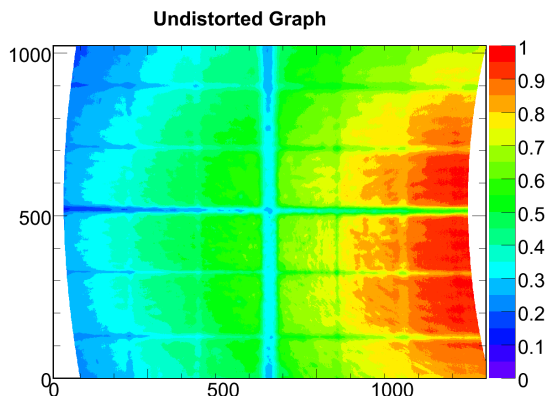


Figure 2.21: This image shows the result of applying the undistortion routine to the distorted image of graph paper in Figure 2.16.

that are closer to a particular image point.

In either method, once the polynomial co-efficients are determined, they can be applied to any image taken in the same system with the calibration foil replaced. To test the undistortion routine, the foil is replaced with graph paper producing the image shown in Figure 2.16. The polynomial mapping recovers the straight lines of the graph in Figure 2.21.

## 2.9 Efficiency Correction

The image of the proton beam will span most of the foil and thus its centroid will be affected by the efficiency dropoff observed in Figure 2.17. A reliable efficiency correction routine is required to fix this. Since the camera (Section 2.3) and light source (Figure 2.14(b)) entering the system are uniform, we know that the efficiency map observed in Figure 2.17 is a consequence of only the mirrors and the apertures of the optical system. Thus, as long as the angular distributions of light are similar, any other images from this system can be corrected using this efficiency map.

The correction is performed by dividing the intensity of a pixel in an image by

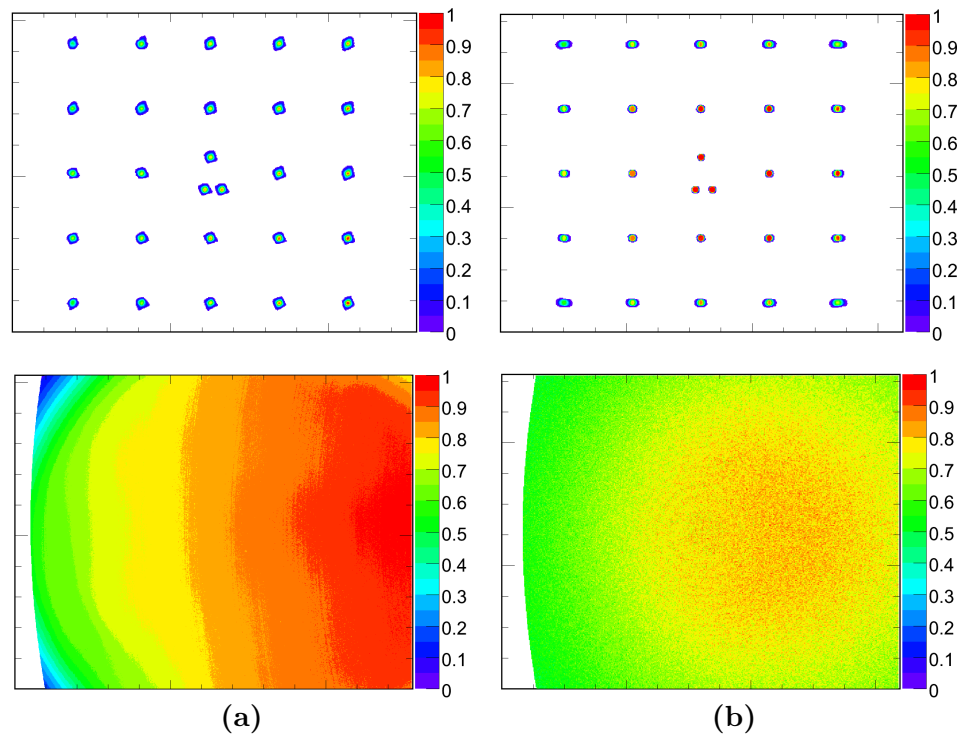


Figure 2.22: The undistorted grid of control points (top) and corresponding efficiency map (bottom) ‘for (a) the prototype and (b) the simulated system. The difference in the efficiency maps is due to slight misalignments in the prototype and a different angular distribution of light in the simulation. The source was programmed to be at the position of the foil while in the prototype the source was a meter behind the foil. This is not a problem for correction since one map will not be used to correct the other grid. Note the graininess of the simulated efficiency map is due to insufficient statistics.

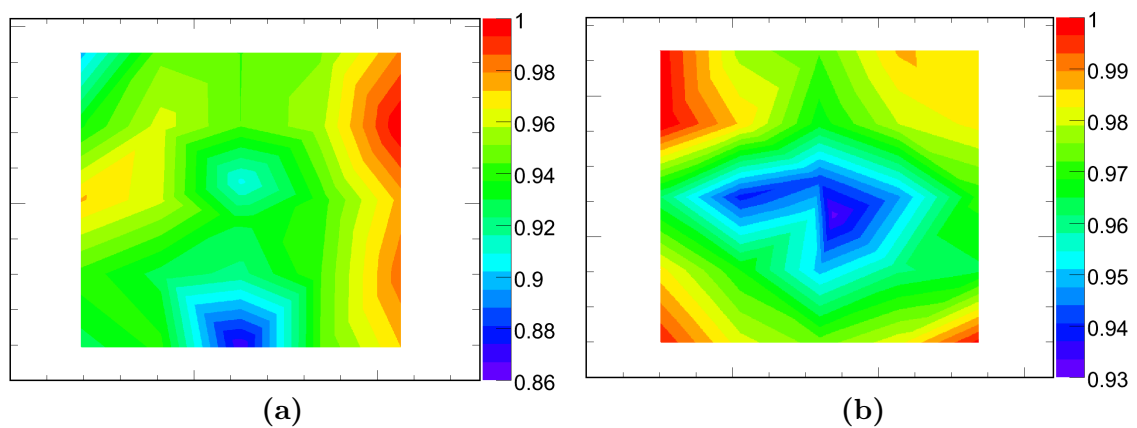


Figure 2.23: The Delaunay interpolation of the grids in Figure 2.22 after they have been efficiency corrected. (a) Prototype (b) Simulated.

the corresponding pixel in the efficiency map. The images used to test this routine are the undistorted images of the prototype and simulated grid holes shown in Figure 2.22 with the corresponding efficiency map. To better observe the correction, the intensities in the region between the holes were calculated using Delaunay interpolation and plotted in Figure 2.23. Since the grid is generated from the exact same light source that generated the efficiency map, the resulting image is expected to be flat. However, there is still some residual radial bias which is a consequence of the small amount of holes per unit area leading to error in the interpolation. But overall, the 50% gradient in the efficiency maps has been reduced to about 5% in the corrected images.

With confidence in the undistortion and efficiency correction routines, they can now be applied to simulations of a real proton beam in the full-sized system.

## Chapter 3

# Beam Reconstruction Simulations

To test the effectiveness of the undistortion and efficiency correction routines, they are applied to a simulated image of an actual beam profile<sup>1</sup>. In the beam simulation code [8], the starting position of a proton is given by a two-dimensional Gaussian of width 7.5 mm, centered at a user-defined position. The direction of all the protons within the beam are the same, along the beam axis.

For a shiny foil at  $45^\circ$ , the perfect reflection axis would be at  $90^\circ$ . However, in the full-sized system a titanium alloy (15-3-3-3) foil will likely be used which has some roughness producing diffuse reflection. This was quantified in the lab by shining a laser at a sample of the foil and measuring the intensity of reflected light at various angles. In the simulation, a random ‘diffuse angle’ is picked according to the measured distribution of the fitted data in Figure 3.1 (see Appendix B). Also, an OTR angle is picked randomly according to the distribution given in Figure 1.5. The diffuse angle and the OTR angle are added to give the initial direction of the light ray emanating from the proton’s intersection point on the

---

<sup>1</sup>Example images of the beam profile at each stage of correction are given in Appendix C.

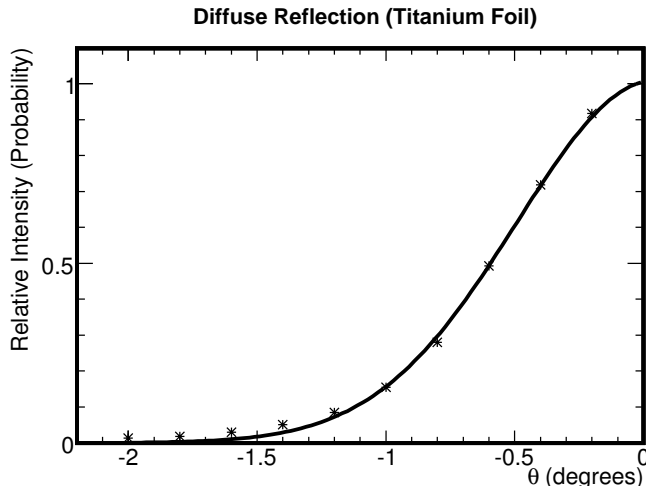


Figure 3.1: This plot shows the intensity distribution of reflected light from a titanium alloy (15-3-3-3) foil, where  $\theta$  is the deviation from a perfect reflection axis. The points are fit to a Gaussian of width  $0.55^\circ$ . For comparison, the shiny side of aluminum foil was measured with a width of  $0.25^\circ$  and the dull side at  $6.8^\circ$ .

foil. Finally, this ray is traced through the optical system with the parameters set to match the dimensions of the full-sized system.

### 3.1 Lighting

As described in Figure 2.22, the angular distribution of light used to generate an efficiency map is important. Variations in the angular distribution can actually change the shape of the efficiency map by a significant amount, and thus affect the results of the efficiency corrections. To understand the effects of this, three distortion and efficiency maps were generated from three different angular distributions: OTR plus diffuse reflection,  $3^\circ$  uniform cone and a  $10^\circ$  uniform cone (simulating these cones is discussed in Appendix B). The OTR plus diffuse reflection distribution represents the case that the proton beam (as

wide as the foil, at very low intensity) is directed at the calibration foil to produce OTR light. The  $3^\circ$  cone is analogous to a back-lighting source far away from the foil. The  $10^\circ$  represents front-lighting or a nearby back-lighting source.

In the following discussion, the OTR plus diffuse reflection distribution will be referred to as ‘OTR’, the  $10^\circ$  cone as ‘Cone’ and the  $3^\circ$  cone as ‘Mono’ (directional).

## 3.2 Undistortion

Twenty-one beam positions on the foil (Figure C.1 is an example of one) were simulated by translating the position (in mm) of the beam center diagonally from  $(x, y) = (-10, -10)$  to  $(x, y) = (10, 10)$  in integer steps. Three distortion maps were generated from a 9 by 9 grid of point sources of light using each angular distribution. The undistortion routine, using each distortion map, was applied to the distorted image of the beam profiles (Figure C.2) to produced an undistorted image (Figure C.3). The center position is calculated by fitting a 2-D Gaussian to the beam profile. Figure 3.2 shows that even after undistortion, the reconstructed beam positions are still heavily biased toward the center due to the efficiency drop of the system and thus require efficiency correction.

## 3.3 Efficiency Correction

A second method for producing an efficiency map (Section 3.3.1) was tested in addition to the method previously described. Both methods were applied using the three angular distributions. Simulations result in a circular shaped efficiency map (Figures 3.3 and 3.12) that drops off to zero around the the edges. Table 3.1 summarizes the mean center position

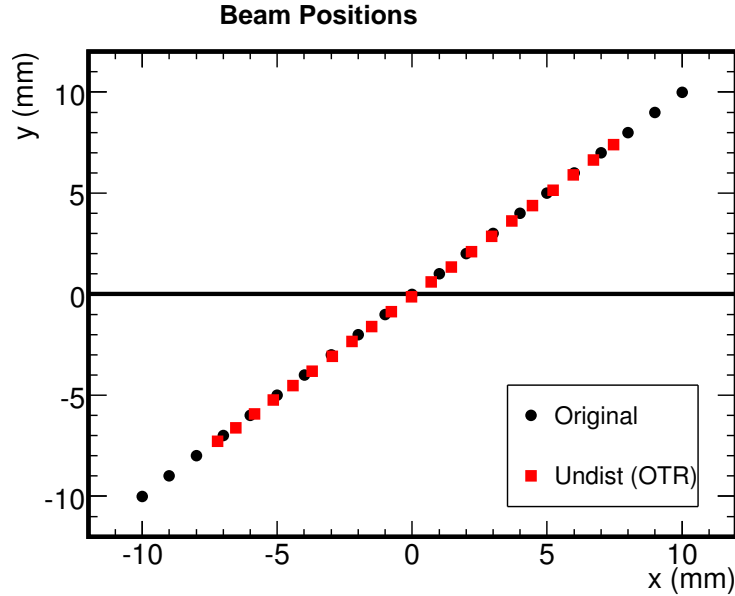


Figure 3.2: The three distortion maps corresponding to the different angular distributions are all very similar and so only the results of one are shown.

	'Grid' Method			'Disk' Method		
	<b>OTR</b>	<b>Cone</b>	<b>Mono</b>	<b>OTR</b>	<b>Cone</b>	<b>Mono</b>
Mean x	0.1691	0.2001	0.2005	-0.19	-0.192	-0.194
Mean y	0.2112	0.1974	0.1955	0.2116	0.1987	0.1959
RMS x	11.53	11.51	11.52	11.48	11.44	11.46
RMS y	11.50	11.47	11.92	11.43	11.41	11.42

Table 3.1: This table compares the characteristics of the efficiency map histograms created using the two methods in the following section. All quantities are in mm.

and RMS of each map.

### 3.3.1 Efficiency Map produced from a Grid

A grid of 21 by 21 points was simulated. A random direction was chosen based on the angular distribution used. A ray was generated at each point with the same direction. The ray was traced through the optical system and tallied if it was imaged, regardless of where it hit the camera. After repeating this procedure several times, each true grid point

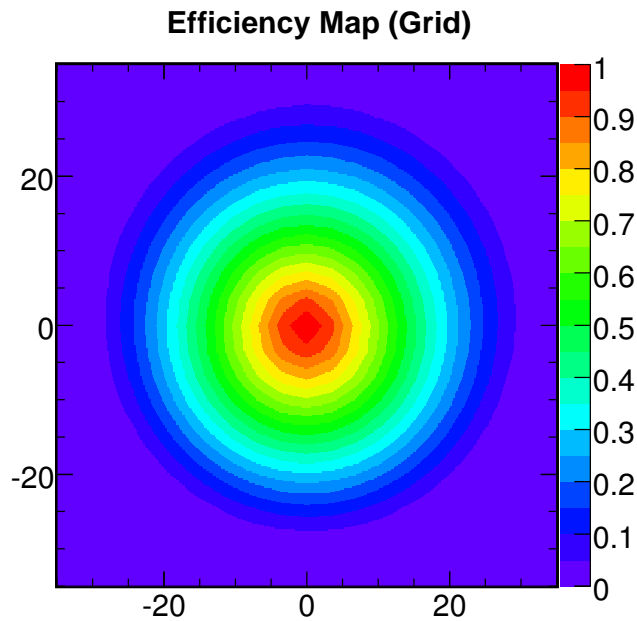


Figure 3.3: Efficiency Map Created from a Grid

position was assigned an efficiency value corresponding to the amount of rays that were imaged at the camera from that point. Finally, bilinear interpolation was performed to obtain an efficiency value for all points in between the grid, producing the efficiency map shown in Figure 3.3. In the real system, this simulation is analogous to the case of using a back-lit grid of holes to produce an efficiency map. The undistorted beam profiles were then efficiency corrected using these efficiency maps.

Figure 3.4<sup>2</sup> shows that with this method, the reconstructed beam positions begin to diverge further away from the center. This is because the generated efficiency map does not take into account the effect of distortion and blurring of the image. Basically, this is correcting an image in camera space with an image in foil space. Consider a circular region

<sup>2</sup>Most of the beam positions in the first quadrant are not calculated because the fitting routine failed for an undetermined reason.

of equally intense pixels in foil space that sum to some total intensity. After traveling through the optical system, the blurring and distortion will produce a larger area in camera space with the same total intensity. This corresponds to a lower observed intensity value (lower efficiency) per pixel. Generating the efficiency map based on a grid does not take into account this blurring and distortion, causing the edges of the map to appear more efficient than they should<sup>3</sup>. This accounts for the fact that the reconstructed positions are pushed radially inward in Figure 3.4.

Figures 3.5 and 3.6<sup>4</sup> show the horizontal (x) and vertical<sup>5</sup> (y) deviation of the reconstructed beam position from the actual beam position. The reconstructed width of the beam is plotted in Figure 3.7 showing the same radial trend as the previous plots.

### 3.3.2 Efficiency Map produced from a Uniform Disk

In the real full-sized system, the method used in the prototype system (Section 2.9) is analogous to front-lighting a blank foil or back-lighting an empty foil holder. Even after undistortion, the efficiency map obtained is essentially an image in camera space which includes the blurring and distortion effects. The graininess of the efficiency map in Figure 2.23(b) is also present in the full-sized simulations and is corrected by using a smoothing routine<sup>6</sup> to produce Figure 3.12. Correcting the images, which are also in camera space, using this map eliminates the previous radial bias (Figure 3.8). As well, the deviations in position and width, shown in Figures 3.9, 3.10 and 3.11, are much smaller.

---

<sup>3</sup>This corresponds to the larger RMS observed in Table 3.1

<sup>4</sup>Negative  $r$ 's correspond to points in the third quadrant of Figure 3.4 while positive  $r$ 's correspond to the first quadrant.

<sup>5</sup>Note that the distortion is in the vertical direction now that we are dealing with the full-sized system and not the prototype.

<sup>6</sup>Each pixel is assigned a value equal to the average of itself and the 8 surrounding pixels.

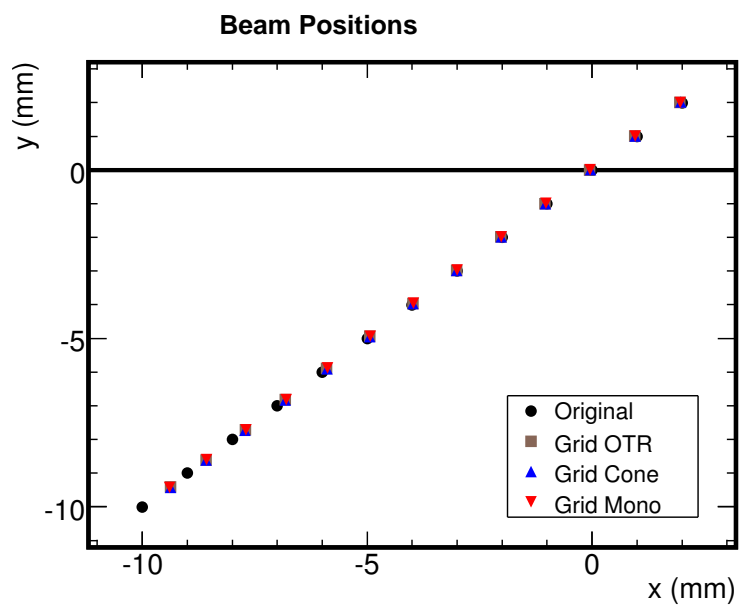


Figure 3.4: Efficiency Corrected Beam Positions (Grid Map)

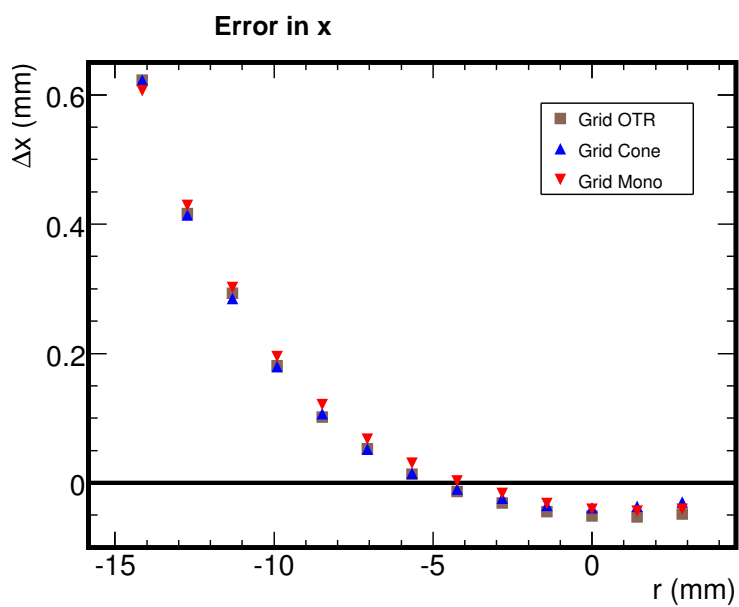


Figure 3.5: Error in x using a Grid Efficiency Map

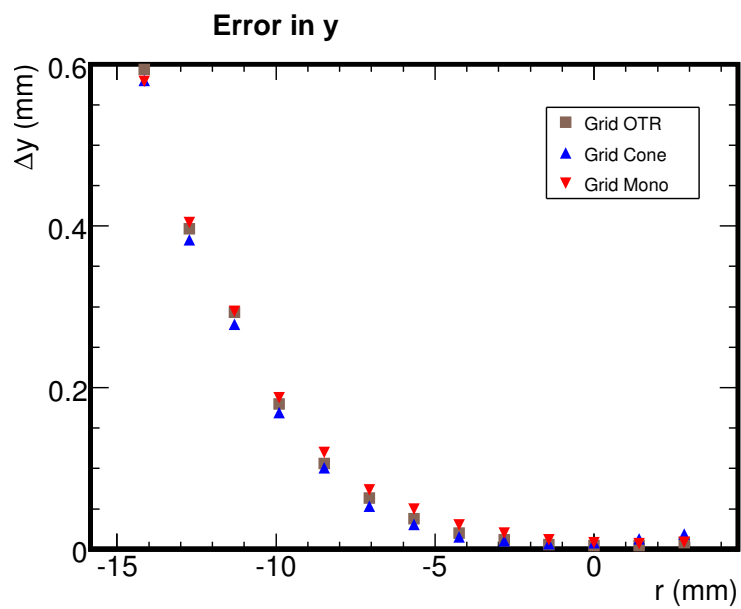


Figure 3.6: Error in y using a Grid Efficiency Map

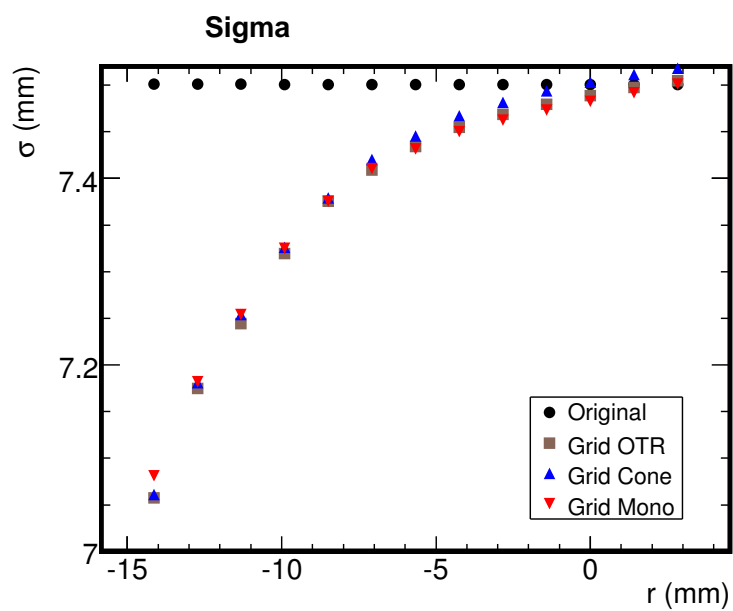


Figure 3.7: Reconstructed Width using a Grid Efficiency Map

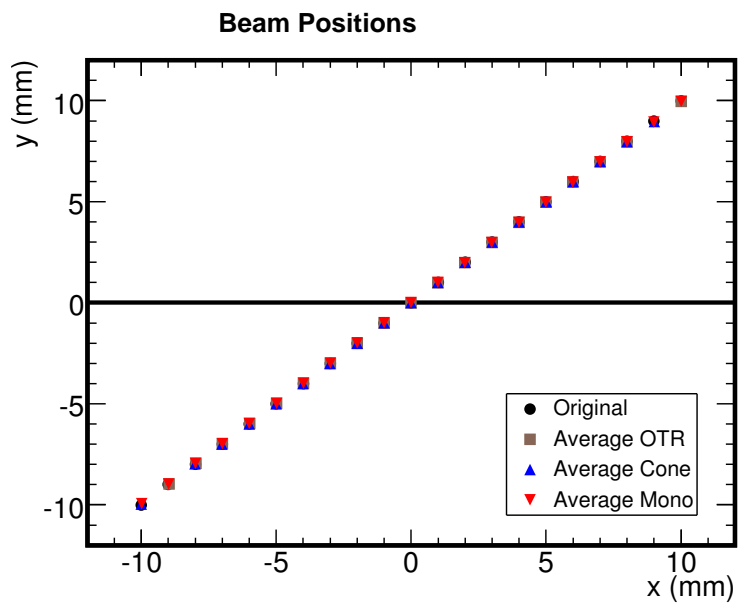


Figure 3.8: Efficiency Corrected Beam Positions (Disk Map)

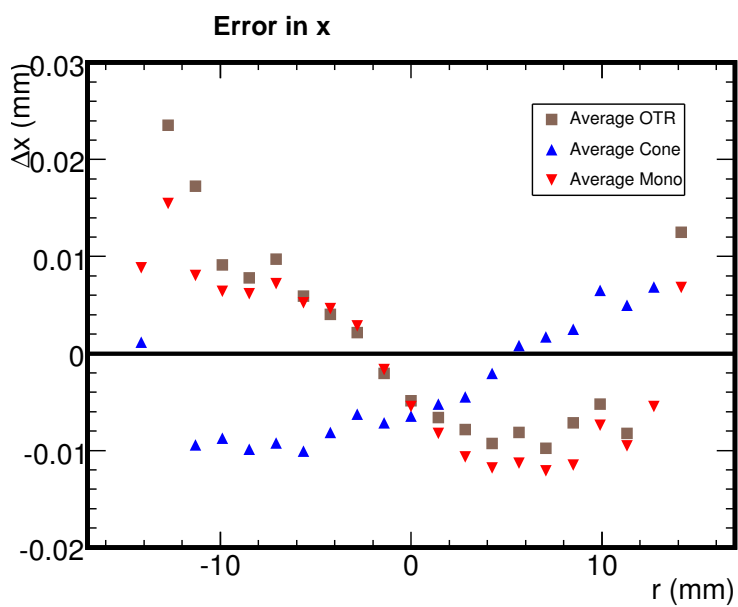


Figure 3.9: Error in x using a Disk Efficiency Map

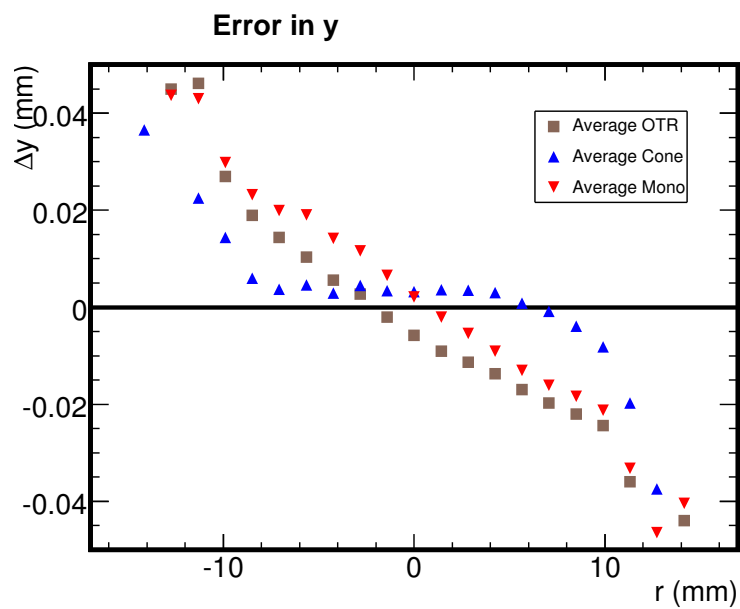


Figure 3.10: Error in y using a Disk Efficiency Map

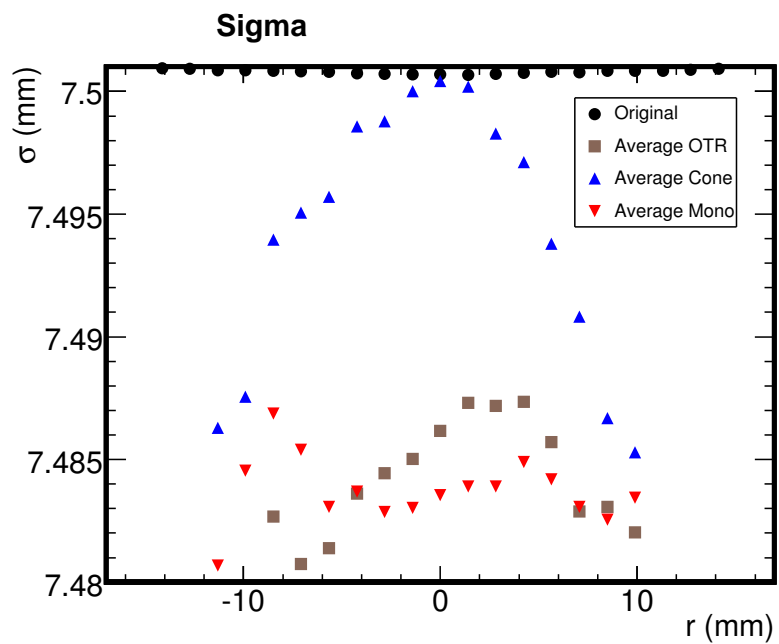


Figure 3.11: Reconstructed Width using a Disk Efficiency Map

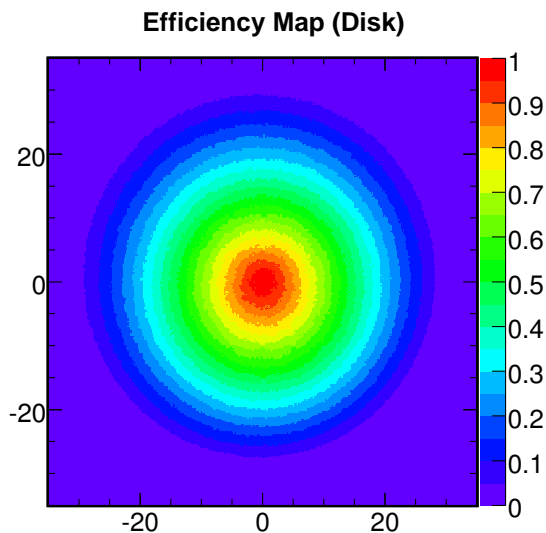


Figure 3.12: Efficiency Map Created from an Empty Foil Holder (Uniform Disk)

Any observable trends in these plots are likely attributable to the low statistics in producing the efficiency maps, otherwise the deviations are constant as the radius is varied.

### 3.4 Results

Within either efficiency correction method, the difference between the effects of each of the angular distributions is negligible. Table 3.1 shows that there is some uncertainty between the distributions, comparable in size to the differences observed in the error plots. This suggests that any method of lighting, as long as it is uniform across the foil, is sufficient for generating an efficiency map. Table 3.2 shows the upper bound of errors in the beam reconstruction at an extreme position<sup>7</sup> of the foil, 10 mm away from the center of the foil. The results at a more reasonable beam position, 2 mm away from the center, are shown in

<sup>7</sup>A beam centered at this position will have already hit the sides of the collimator causing problems not of the concern of the OTR monitor.

Table 3.3. Using the grid method results in a larger deviation further away from the center compared to using the disk method. Close to the center, the two methods show similar results. Compared to the grid method, the disk method reconstructed the beam position and width more accurately regardless of the position on the foil.

	<b><u>'Grid' Method</u></b>	<b><u>'Disk' Method</u></b>
$\Delta x$	0.2	0.01
$\Delta y$	0.2	0.03
$\Delta \sigma$	0.2	0.02

Table 3.2: This table shows the maximum error in the reconstructed position and width of the beam, 10 mm away from the center. (Quantities are in units of mm.)

	<b><u>'Grid' Method</u></b>	<b><u>'Disk' Method</u></b>
$\Delta x$	0.05	0.01
$\Delta y$	0.02	0.01
$\Delta \sigma$	0.05	0.017

Table 3.3: This table shows the maximum error in the reconstructed position and width of the beam, 2 mm away from the center. (Quantities are in units of mm.)

## Chapter 4

# Conclusions and Recommendations

### 4.1 Conclusions

The OTR monitor serves as a target protection device as well as a beam profile measurement device for physics purposes. The beam must be shut off if the measured width exceeds or falls short of established thresholds. A measurement of the position can aid in predictions of the beam direction. The monitor must be assembled and calibrated to reconstruct beam positions and widths to within 0.5 mm to serve these purposes.

The accuracy of the monitor depends on several factors. The optical system alignment is crucial to obtaining well-behaved and easily analysed images. Deviations in a mirror by even 0.5 mm can result in images that do not compare to expected distortion and efficiency falloff. A foil with a grid of holes and distinguishable center pattern is sufficient for image processing calibration. The lighting across the foil and the camera must be uniform (or known) to produce an accurate efficiency map for later corrections. Back-lighting is more effective than front-lighting for calibration.

An image processing and correction procedure has been developed and tested. The image processing procedure for real images consists of an adaptive thresholding routine, hole finding, pattern recognition and hole matching routines. The correction procedure consists of an undistortion and efficiency correction routine. Both procedures were tested with the prototype system with the correction routines accurate to 5%. The correction procedure was also tested on simulated beam images reconstructing the beam positions and widths accurate to 0.03 mm, well within the target goal of 0.5 mm. So the only limitations that remain in the full-sized system now are those factors mentioned above.

## 4.2 Recommendations

Several recommendations for the full-sized system were made throughout this document. This section will summarize those as well as suggest more that are applicable to the full-sized system once it begins assembly and alignment at the University of Toronto.

For the initial assembly, an optical table can be used to characterize the center of each mirror, however the system will be too large to place entirely on the table. The centers of the mirrors should also be well-defined by the manufacturer so that installation can be accurate. Fine-tuning the mirrors within the pipe by finding the  $90^\circ$  reflection point still requires discussion. The entire system must then be aligned to the beam axis in Japan. Some discussion has been made of employing surveyors on-site for this purpose. Since it may be difficult to align a laser at the bottom of the system to test the alignment, it can also be tested by replacing the foil with a flat mirror at  $90^\circ$  and shining a laser from the camera position at the top and using the back-reflection as a reference.

In the prototype system, the foil was large enough to fit a full rectangular grid. However, in the full-sized system it is ideal to fill the entire foil with a square grid, but since the foil is circular the corner holes of the grid will be cut off. The hole matching routine works outward from the center and is not limited by this. The holes should also be scaled up to allow sufficient light through. To produce the most accurate distortion map, the amount of holes should be maximized while still being able to distinguish the center pattern.

Lighting is likely to be the primary limitation in the system. In the prototype system, it is easy to setup uniform back and front-lighting sources, however in the full-sized system we are constrained by the physical design and dimensions. Light sources can only be placed in certain locations. There are two options currently available: radiation-hard filaments near the foil and a light-pipe coming from the top. Each filament should be mounted within a diffuse parabolic reflector to focus the light onto the foil. The light-pipe will have to be followed by a series of mirrors, all of which are shiny except a diffuse mirror preceding the foil. The uniformity of the light at the position of the foil should be tested as it may vary greatly depending on the positioning of the light source. In Japan, it is advised to make this measurement and include it in the efficiency maps if it is far from uniform. The camera is expected to be uniform (but should still be tested) and will not affect the efficiency maps.

A foil holder should be left empty, for the purpose of aligning the foil to the beam axis using a laser and also for obtaining an accurate efficiency map from back-lighting. If this is impossible, obtaining an efficiency map from the back-lit grid is still possible if we can

afford the loss of accuracy. An empty foil holder can still be aligned before the installation of an actual foil. An efficiency map can also be obtained by front-lighting a non-calibration foil.

## Appendix A

# Hole Matching Code

The following code, written in C++, is appended to the hole finding code [9] and runs within the same process. The main function, ‘LabelGrid’ (Line 224), takes as input the  $(x, y)$  co-ordinates of the centroids. First the routine ‘FindCenter’ (Line 121) is called to identify the center triangle pattern. The center of the triangle is calculated and defined as the origin and labeled as the middle row and column. The center of the simulated control points is defined to be in the center of the image, however if the origin is off-center, all the control points are translated accordingly<sup>1</sup> (Lines 184-204).

All the centroids in the center column are labeled using the ‘LabelRow’ routine (Line 3) which finds neighbouring vertical points using a distance threshold. The ‘cursor’ is moved to the next column to the right using the ‘NextColumn’ routine (Line 69) which also uses a distance threshold to find the closest point in the next column. This is repeated until the cursor reaches the last column, after which it proceeds to the first column to the

---

<sup>1</sup>This is done only to better observe the differences in the positions in situ. In principle, the undistortion routine (Section 2.8) is capable of performing this translation.

left of the center column. All the centroids are labeled by moving the cursor to the left for all the remaining columns.

```

1  /*=====LABEL ROW=====*/
   //repeatedly used in Grid Labeling routine
3  void LabelRows(HoleStruct *Hole, HoleStruct &CurrentHole) {
5      int i;
7      row = 1; //start labeling rows above the center row
9      //label each point above the center in the current
   //column by its row number
11     for (i=0; i < nGridHoles; i++) {
13         if ( Hole[i].ignore==false
14             //ensure hole is within the same column
15             && abs(Hole[i].xCoord - CurrentHole.xCoord) < xUncert
16             //ensure hole is above the current hole
17             && (Hole[i].yCoord - CurrentHole.yCoord) > 0.
18             //ensure hole is neighbouring
19             && abs(Hole[i].yCoord - CurrentHole.yCoord) < yRange ) {
21             Hole[i].rowLabel = row; Hole[i].colLabel = col;
22             Hole[i].ignore = true;
23             CurrentHole = Hole[i];
25             i=-1; //to cycle through all the points again
26             row++; //proceed to next row
27         }
28     }
29     //go back to the center row of the current column
30     for (i=0; i < nGridHoles; i++)
31         if (Hole[i].rowLabel == 0 && Hole[i].colLabel == col)
32             CurrentHole = Hole[i];
33
34     row = -1; //start labeling rows below the center row
35
36     //label each point below the center in the
   //current column by its row number
37     for (i=0; i < nGridHoles; i++)
38         if ( Hole[i].ignore==false
39             //ensure hole is within the same column
40             && abs(Hole[i].xCoord - CurrentHole.xCoord) < xUncert
41             //ensure hole is below the current hole
42             && (Hole[i].yCoord - CurrentHole.yCoord) < 0.

```

```

45         //ensure hole is neighbouring
         && abs(Hole[i].yCoord - CurrentHole.yCoord) < yRange ) {
47
         Hole[i].rowLabel = row; Hole[i].colLabel = col;
49         Hole[i].ignore = true;
         CurrentHole = Hole[i];
51
         i=-1; //to cycle through all the points again
53     row--; //move label to next row
    }
55
    //go back to the center row of the current column
57     for (i=0; i < nGridHoles; i++)
        if (Hole[i].rowLabel == 0 && Hole[i].colLabel == col)
59         CurrentHole = Hole[i];
        row = 0;
61
    //proceed to next column
63     if ( col>=0 ) col++; //move label to next column to the right
        else if ( col<0 ) col--; //move label to next column to the left
65 }

67 /*=====NEXT COLUMN=====*/
    //repeatedly used in Grid Labeling routine
69 void NextColumn(HoleStruct *Hole, HoleStruct &CurrentHole) {

71     int i;

73     //assuming we're on the right side of the grid
    if ( col>0 ) {
75         //move to the next point to the right of the
            //current column's center row point
77         for (i=0; i < nGridHoles; i++) {
            if ( Hole[i].ignore==false
79                 //ensure hole is within the same row
                && abs(Hole[i].yCoord - CurrentHole.yCoord) < yUncert
81                 //ensure hole is to the right
                && Hole[i].xCoord - CurrentHole.xCoord > 0
83                 //ensure hole is neighbouring
                && abs(Hole[i].xCoord - CurrentHole.xCoord) < xRange ) {
85
                Hole[i].rowLabel = 0; Hole[i].colLabel = col;
87                 Hole[i].ignore = true;
                CurrentHole = Hole[i];
89
                break; //stop before it finds the next point to the right
91             }
        }
93     }

```

```

95 //assuming we're on the left side of the grid
else if ( col<0 ) {
97
    //move to the next point to the left of the center point
99    for (i=0; i < nGridHoles; i++) {
        //ensure hole is within the same row
101        if ( abs(Hole[i].yCoord - CurrentHole.yCoord) < yUncert
            //ensure hole is to the left
103            && Hole[i].xCoord - CurrentHole.xCoord < 0
            //ensure hole is neighbouring
105            && abs(Hole[i].xCoord - CurrentHole.xCoord) < xRange ) {
107            Hole[i].rowLabel = 0; Hole[i].colLabel = col;
            Hole[i].ignore = true;
109            CurrentHole = Hole[i];
111            break; //stop before it finds the next point to the left
        }
113    }
    }
115 }

117 /*=====FIND CENTER OF GRID=====*/
    //can be changed to suit specific center pattern:
119 //Pattern: triangle with vertices:
    //          (0, 0.3),(-0.1,-0.3),(0.2,-0.3) mm
121 void FindCenter(HoleStruct *Hole, HoleStruct &RefHole) {
123     int i,j,k=0;
125     const int nCenter = 3; //number of holes in center pattern
    double centerI=0; //average intensity of center of grid
127     double totalWeight=0; //for weighted average
    float xTrans=0; //for translating origin of grid
129     float yTrans=0; //to exact image center
131     nGridHoles = nHoles - nCenter + 1;
    GridHole = new HoleStruct[nGridHoles];
133     HoleStruct CenterHole[nCenter]; //array of holes in center pattern
135     //factors depends on the dimensions of above pattern
    const double xMaxSpace = xGridSpace*0.4;
137     const double yMaxSpace = yGridSpace*0.6;
    float topCoordy; //y-coordinate of top-center hole (pixel)
139     float bottomCoordy; //y-coordinate of bottom-center holes (pixel)
141     //Find all the holes in the center pattern and store in array,
    //for each RealHole
143     for (i=0; i < nHoles; i++) {

```

```

145     Hole[i].ignore = true; //don't compare the current hole to itself
147     //compare to every other hole
    for (j=0; j < nHoles; j++) {
149         //If another hole is within the Max Spacing of the center
151         //then it is part of the center.
        //don't compare to itself or previous holes not within center
153         if ( Hole[j].ignore == false
            && abs(Hole[i].xCoord - Hole[j].xCoord) < xMaxSpace
155             && abs(Hole[i].yCoord - Hole[j].yCoord) < yMaxSpace ) {

157             CenterHole[k] = Hole[i];
                Hole[i].ignore = false; //this hole is in center so
159                                     //compare in the next loop

                k++;
161                 break; //don't compare with any following center holes
            }
163     }
}
165
//Find the Origin
167
//initialize center hole for comparison
169 RefHole.yCoord = 0.;

171 //find the highest hole of the pattern to use as
//reference and calculate total intensity
173 for ( k=0; k < nCenter; k++ ) {
    if ( CenterHole[k].yCoord > RefHole.yCoord ) {
175
177         //set reference hole as the topmost center hole
        RefHole = CenterHole[k];

179         //find yCoord of the bottom blotch
        bottomCoordy = CenterHole[(k+1)%nCenter].yCoord ;
181     }
}
183
//Translate highest hole to center of grid
185 //(assuming NO ROTATION OF IMAGE)
RefHole.yCoord = RefHole.yCoord - (RefHole.yCoord-bottomCoordy)/2;
187
//calculate average intensity of center of grid
189 RefHole.nHits =
    ( CenterHole[0].nHits + CenterHole[1].nHits
191     + CenterHole[2].nHits) / 3;

193 //label the center
RefHole.ignore = true; RefHole.rowLabel = 0; RefHole.colLabel = 0;

```

```

195 //calculate center offset of image grid to control grid
197 xTrans = xRes/2 - RefHole.xCoord;
    yTrans = yRes/2 - RefHole.yCoord;
199
    //translate all the control points by the offset
201 for (i=0; i<nPoints; i++) {
    ControlPoint[i].xCoord = ControlPoint[i].xCoord - xTrans;
203 ControlPoint[i].yCoord = ControlPoint[i].yCoord - yTrans;
    }
205
    GridHole[0] = RefHole; //put the origin into the grid array
207 j=1; //start labeling the grid array after the origin

209 //place all the non-center holes into the grid array
    for ( i=0; i < nHoles; i++ ) {
211         if ( Hole[i].ignore == true ) {
            GridHole[j] = Hole[i];
213
                //initialize labels for comparison
215 GridHole[j].rowLabel = nGrid;
                GridHole[j].colLabel = nGrid;
217 GridHole[j].ignore = false;
                j++;
219         }
    }
221 }

223 /*=====LABEL GRID=====*/
    void LabelGrid() {
225
        int i;
227
        //declare and initialize variable to store
229 //center point (reference hole)
        HoleStruct RefHole;
231
        //Find center hole
233 FindCenter(RealHole,RefHole);

235 //initialize comparison point to be center point
        HoleStruct CurrentHole = RefHole;
237

239 //label all points on the RIGHT half of the grid
        while ( col <= (nGrid-1)/2 ) {
241
            //Label all the rows in the current column
243 LabelRows(GridHole,CurrentHole);

```

```
245     //Proceed to the next hole in the center row
      NextColumn(GridHole,CurrentHole);
247 } //end while (right half of grid)
249
251 //Now start at the column to the left of the center
      CurrentHole = RefHole;
253 col = -1;
      NextColumn(GridHole,CurrentHole);
255
257 //label all points on the LEFT half of the grid
      while ( col >= -(nGrid-1)/2 ) {
259         //Label all the rows in the current column
261         LabelRows(GridHole,CurrentHole);
263         //Proceed to the next hole in the center row
          NextColumn(GridHole,CurrentHole);
265     } //end while (LEFT half of grid)
267
      //Make row/col labels all >= 0
269     for (i=0; i<nGridHoles; i++) {
          GridHole[i].rowLabel += (nGrid-1)/2+1;
271         GridHole[i].colLabel += (nGrid-1)/2+1;
      }
273 }
```

## Appendix B

# Diffuse Light and Uniform Cone Code

```

2 //double coneAng = <desired opening angle of cone>;
u1 = 1 - ( ( 1 - (cos(coneAng)+1)/2 ) * gRandom->Rndm() );
randTheta = acos(2*u1-1);
4 //where cos(randTheta) is uniform on (2*u1-1)
randPhi = gRandom->Rndm() * 2*PI;
6
randI = gRandom->Rndm();
8 if ( randI <= exp( -(randTheta-0)/2*(randTheta-0)/2 /
(2*diffSigma*diffSigma) ) ) {
10
//Beam code and raytracing code, etc. goes here.
12 }

```

This snippet of code is an implementation of the uniform cone distribution, or ‘isotropic direction in 3D’, described in [11]. Lines 2-5 determines the direction of the photon relative to the center axis of the cone. ‘u1’ is chosen randomly according to the distribution which then defines ‘randTheta’, the polar angle between the photon and the center axis of the cone. The azimuthal angle, ‘randPhi’, is randomly chosen uniformly from

0 to  $2\pi$ . These two angles then define the direction of the initial ray. This is used for the uniform cone light distributions (Section 3.1) as well as for the diffuse reflection (Section 3) code.

Picking the angle for the diffuse reflection uses the ‘acceptance-rejection’ method [11] on the distribution determined in Figure 3.1, where ‘diffSigma’ is the width of the Gaussian fit. If a randomly chosen intensity, ‘randI’, lies below the graph it is accepted, otherwise it is ignored (Lines 7-9).

## Appendix C

# Beam Profiles

The images in this Appendix correspond to Section 3. The difference in the corrected beam profiles between the different methods and angular distributions is unobservable so only one set of images is shown here.

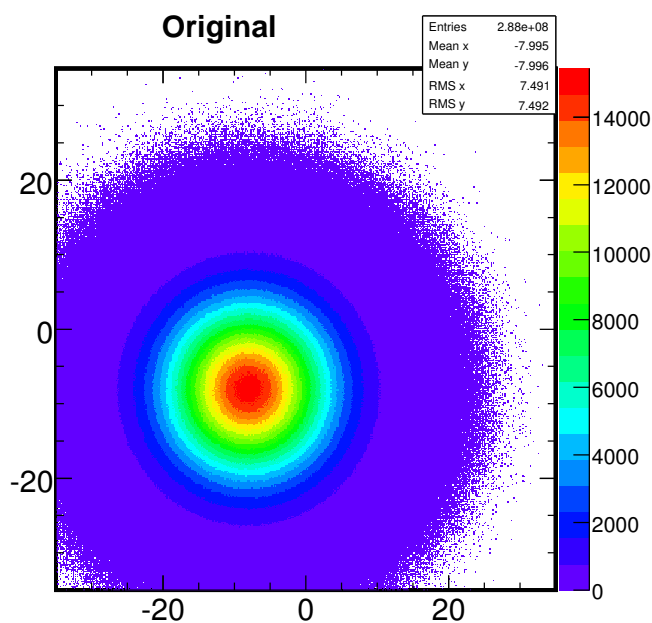


Figure C.1: The original beam profile is a 2D Gaussian of width 7.5 mm. This particular example is centered on  $x = -8$  mm and  $y = -8$  mm.

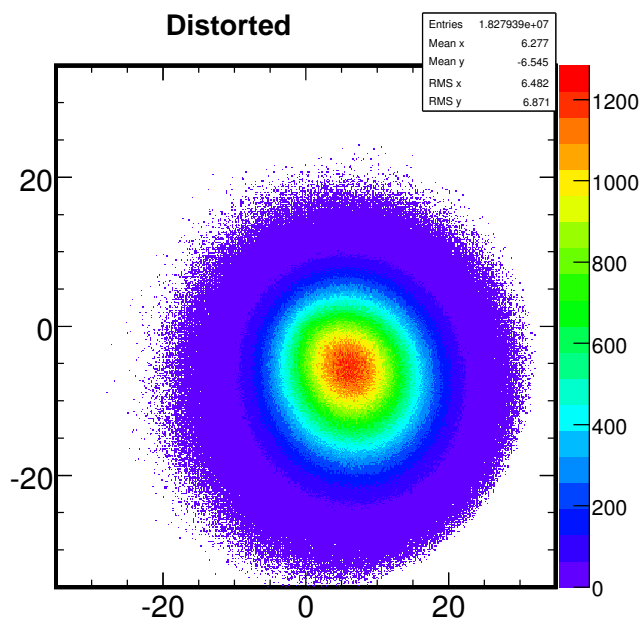


Figure C.2: This image shows the distortion and efficiency falloff effects of the optical system on the beam profile (including a horizontal flip). Notice the non-circular shape and the biased center position. The bottom-right corner of the image is cut off by the pipes in the system.

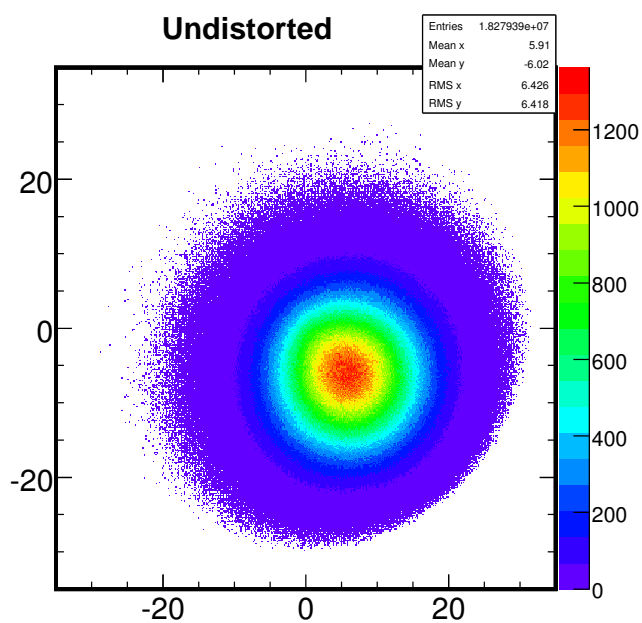


Figure C.3: The undistortion routine recovers the circular shape, however the center is still biased toward the center due to the efficiency falloff.

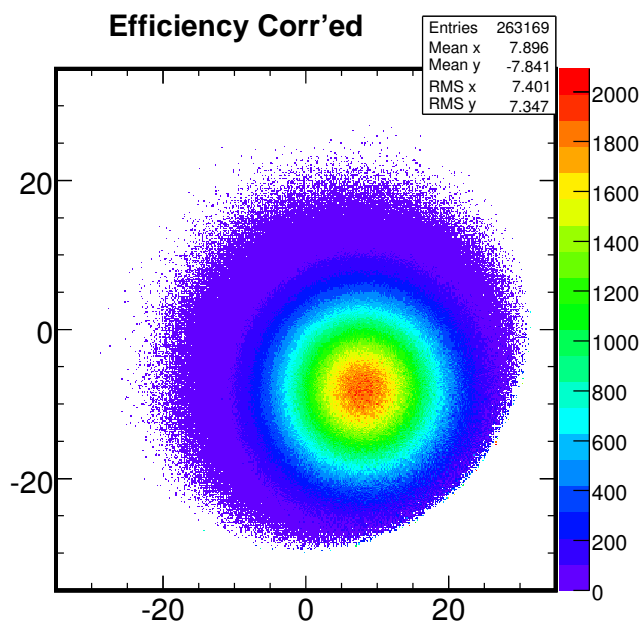


Figure C.4: Applying the efficiency correction, the center is pulled outward, reconstructing the position and width to within tolerance.

# Bibliography

- [1] C. L. Cowan. Detection of the Free Neutrino: a Confirmation. *Science*, 124(3212):103–104, July 20, 1956.
- [2] John N. Bahcall and M. H. Pinsonneault. What Do We (Not) Know about Solar Neutrino Fluxes? *Phys. Rev. Letters*, 92(12):698–711, March 2004. Article 121301.
- [3] The SNO Collaboration. Electron energy spectra, fluxes, and day-night asymmetries of  $^8\text{B}$  solar neutrinos from measurements with NaCl dissolved in the heavy-water detector at the Sudbury Neutrino Observatory. *Phys. Rev. C*, 72, November 2005. Article 055502.
- [4] Super Kamiokande Collaboration. Three flavor neutrino oscillation analysis of atmospheric neutrinos in Super-Kamiokande. *Phys. Rev. D*, 74, August 2006. Article 032002.
- [5] Jay A. Shecker and David Kestenbaum. Celebrating the Neutrino. *Los Alamos Science*, 25, 1997.
- [6] The T2K Collaboration ND280 group. T2K ND280 Conceptual Design Report. pages 1–5, November 2005. T2K internal report.

- [7] J. D. Jackson. *Classical Electrodynamics*. John Wiley and Sons, Inc., third edition, 1999.
- [8] The T2K Collaboration OTR Group. Technical Design Report for the T2K Optical Transition Radiation Monitor. August 2007. [http://phys01.comp.uvic.ca:8080/t2k/projects/beamline/OTR/otr\\_tdr\\_Aug1-2007.pdf](http://phys01.comp.uvic.ca:8080/t2k/projects/beamline/OTR/otr_tdr_Aug1-2007.pdf).
- [9] D. Teo. OTR Proton Beam Monitor for T2K Experiment - Part II, August 14, 2006. Undergraduate Thesis report, York University. [http://phys01.comp.uvic.ca:8080/t2k/projects/beamline/OTR/Don\\_misalignment\\_analysis\\_Aug15.pdf](http://phys01.comp.uvic.ca:8080/t2k/projects/beamline/OTR/Don_misalignment_analysis_Aug15.pdf).
- [10] V. Galymov. Image Correction Techniques, August 2006. Internal notes. [http://www.hep.yorku.ca/slavic/distortion\\_Aug25.pdf](http://www.hep.yorku.ca/slavic/distortion_Aug25.pdf).
- [11] Particle Data Group. Nuclear and Particle Physics. *Journal of Physics G*, 33:311–312, July 2006.